Along-strike spatial variation in shallow slow earthquake activity in Hyuga-nada, southwest Japan

Satoru Baba[1,2], Shunsuke Takemura[1], Kazushige Obara[1], Akiko Takeo[1], Yusuke Yamashita[3], and Masanao Shinohara[1]

1. Earthquake Research Institute, the University of Tokyo, 1-1-1, Yayoi, Bunkyo-ku, Tokyo, 113-0032, Japan
2. Now at Japan Agency for Marine-Earth Science and Technology, 2-15, Natsushima-cho, Yokosuka, Kanagawa, 237-0061, Japan
3. Miyazaki Observatory, Disaster Prevention Research Institute, Kyoto University, 3884 Kaeda, Miyazaki, Miyazaki, 889-2161, Japan

Corresponding author: Satoru Baba (babasatoru@jamstec.go.jp)

Highlights

- We evaluated energy and moment of slow earthquakes in Hyuga-nada.
- These values as well as migration speed have similar along-strike variations.
- The values are generally smaller near the top of the subducted Kyushu-Palau ridge.
- The along-strike variation can be explained by the difference in stress drop.

Abstract

Hyuga-nada, off the Pacific coast of Kyushu along the Nankai Trough in southwest Japan, is one of the most active slow earthquake regions around Japan. We estimated the energies of tremors and moments of very low frequency earthquakes (VLFEs) in Hyuga-nada using data from a permanent onshore broadband network and temporary ocean bottom seismometer observations. The energies and moments of these slow earthquakes have a similar along-strike variation and are generally larger south of the subducted Kyushu-Palau Ridge than near the top of the ridge. This spatial variation is also related to the characteristics of slow earthquake migration. The along-strike migration speed was faster at initiation in the south, where the moments of slow earthquakes are larger. The along-strike migration of slow earthquake episodes can be characterized by deceleration with a parabolic pattern. Assuming a constant patch size of slow earthquakes, we estimated the stress drops of VLFEs and found that the stress drop in the south of the subducted ridge was approximately four times larger than that near the top of the subducted ridge. This stress drop difference between adjacent regions can cause parabolic migration. According to our observations and physical models, the difference in stress drop could be one of the key factors for the spatial variation in slow earthquake activity associated with the subducted ridge.

Keywords: slow earthquake, shallow tremor, shallow very low frequency earthquake, scaled energy, Nankai Trough, Kyushu-Palau Ridge

1. Introduction

After the discovery of tectonic low frequency tremors by Obara (2002), slow earthquakes, which are fault slips with longer characteristic durations than regular earthquakes with the same seismic moment (Ide et al., 2007), were mainly detected around seismogenic zones on plate boundaries of subduction zones in the world. Seismic slow earthquakes are classified into tremors and low frequency earthquakes (e.g., Shelly et al., 2006) observed in a frequency range of 2–8 Hz, and very low frequency earthquakes (VLFEs) observed in a frequency range of 0.02–0.05 Hz (e.g., Obara and Ito, 2005). Slow slip events (SSEs) are geodetically observed as crustal deformations, with duration ranging from several days to several years (e.g., Dragert et al., 2001; Hirose et al., 1999). The spatiotemporal correlation of these slow earthquake phenomena is known as episodic tremor and slip (ETS; Rogers and Dragert, 2003). The focal mechanisms of slow earthquakes in subduction zones are thrust-type and consistent with those of megathrust earthquakes along plate boundaries. In addition, slow earthquake activity can reflect the stress conditions on the plate boundary around the slow earthquake regions (e.g., Obara and Kato, 2016). Recent studies have revealed that slow earthquakes can potentially trigger megathrust earthquakes (e.g., Kato et al., 2012; Vaca et al., 2018). Thus, studies of slow earthquakes are important for understanding the slip behaviors on the plate boundary and the occurrence mechanism of megathrust earthquakes.[1]

Around the Japanese islands, slow earthquakes occur in shallower and deeper extensions of the seismogenic zone in southwest Japan along the Nankai Trough and in the offshore region of northeastern Japan along the Japan Trench. In Hyuga-nada, off the Pacific coast of Kyushu, VLFEs are the most active around Japan (Baba et al., 2020). In this area, Asano et al. (2015) reported the migration of shallow VLFEs, which can be considered as a proxy for rupture propagation of an SSE (e.g., Bartlow et al., 2011; Ito et al., 2007), in 2010 (Fig. 1a). VLFEs first migrated from 30.5º N to 31.5º N along the strike direction and changed to along-dip migration at the subducted Kyushu-Palau Ridge, which is subducting from the Nankai Trough. Although VLFEs are observed by onshore stations owing to the effective propagation of surface waves along shallower low velocity structures, it is difficult to identify weak signals of shallow tremors in Hyuga-nada using permanent onshore stations. Yamashita et al. (2015) and Yamashita et al. (2021) detected shallow tremors and reported their migrations in Hyuga-nada utilizing temporary ocean bottom seismometers (OBSs) in 2013 and 2015, respectively (Fig. 1b and c). In 2013, tremors migrated twice from 30.3º N to 31.7º N. In 2015, tremors migrated from west to east, north of 31º N and extended near the trench axis (Yamashita et al., 2021). The shallow tremors in Hyuga-nada were temporally correlated with shallow VLFEs (Fig. 2). The spatial distributions of tremors in both 2013 and 2015 were contained by those of VLFEs in 2010.

[1] VLFE – very low frequency earthquake; SSE – slow slip event; ETS – episodic tremor and slip; OBS – ocean bottom seismometer; RMS – root-mean-square; JIVSM – Japan Integrated Velocity Structure Model; CC – cross-correlation coefficient

Temporary OBS observations also revealed a high-resolution distribution of VLFEs. Tonegawa et al. (2020) suggested that the depths of shallow VLFEs near the subducted Kyushu-Palau Ridge are approximately 5 km different from the surrounding area.

The tectonic regime in Hyuga-nada is very characteristic; the Kyushu-Palau Ridge is subducted and the trench axis bends around the subduction of the ridge (Fig. 1). In addition, repeating earthquakes representing quasi-static slips on the plate boundary (e.g., Nadeau and McEvilly, 1999; Uchida et al., 2003) occur in the downdip of shallow slow earthquakes (e.g., Igarashi, 2020; Yamashita et al., 2012). Tectonic conditions can affect the source process, such as the moment rate, of slow earthquakes (Baba et al., 2020; Takemura et al., 2022b, 2022a). To investigate the spatial relationships between slow earthquake activity and tectonic conditions in Hyuga-nada, we quantitatively estimated the spatial variation in the source characteristics of slow earthquakes, such as the energy rate functions of tremors and the moment rate functions of VLFEs, at high spatial resolution using onshore and offshore data.

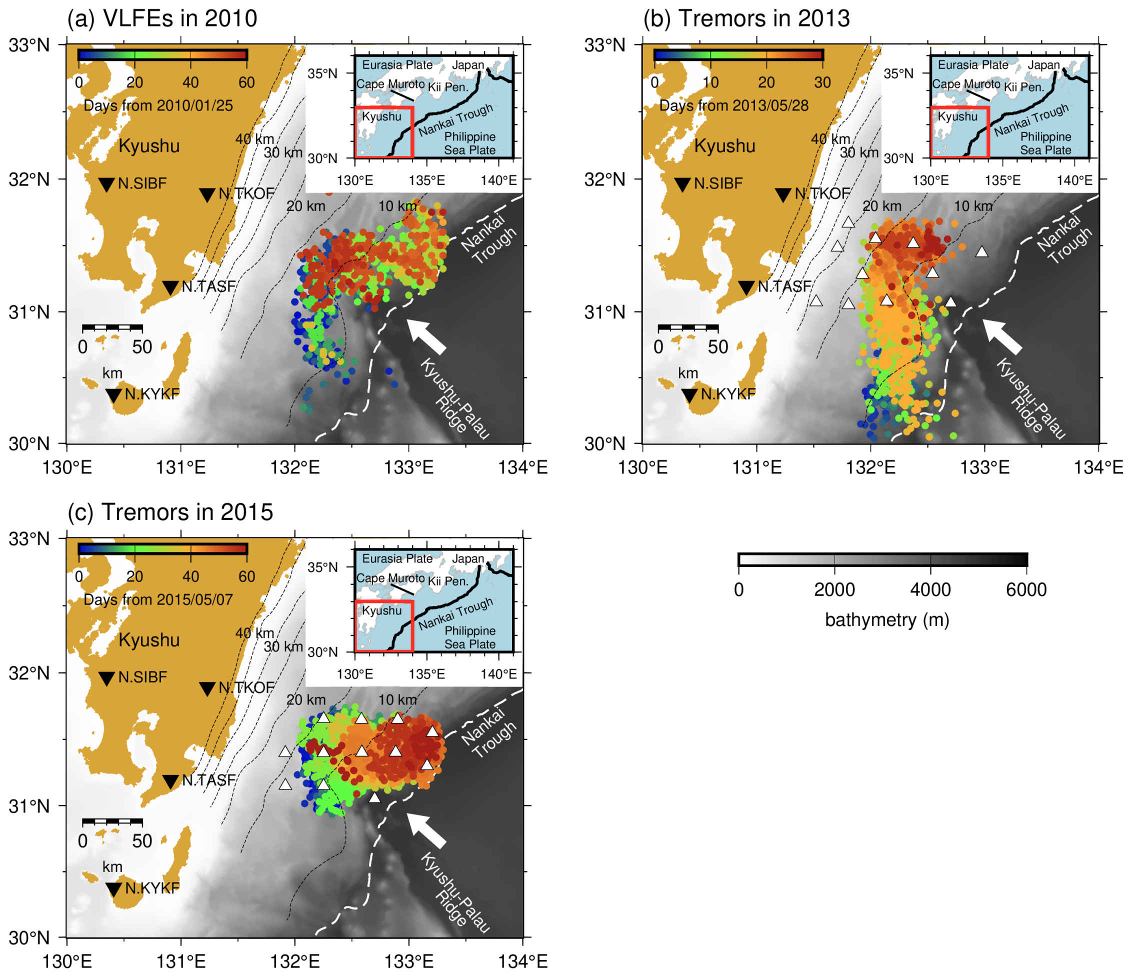

Fig.1. Slow earthquake activity in Hyuga-nada. Colored dots are epicenters of (a) shallow VLFEs in 2010 detected by Asano et al. (2015), (b) shallow tremors in 2013 detected by Yamashita et al. (2015), and (c) shallow tremors in 2015 detected by Yamashita et al. (2021). The colors of dots correspond to days from the first activity for each tremor. White triangles represent the locations of the OBSs utilized in the shallow tremor analysis. Inverted triangles exhibit the locations of the F-net stations utilized in the shallow VLFE analysis. White arrows indicate the direction of the motion of the Philippine Sea Plate relative to the Eurasia Plate (NUVEL-1A; DeMets et al., 1994). White dashed lines represent the trench axis. Background gray scale denotes the bathymetry (ETOPO1; Amante and Eakins, 2009). Dashed contours indicate the isodepth at the top of the Philippine Sea plate in intervals of 5 km (Nakanishi et al., 2018). Black lines in the inset represent the boundaries between the plates.

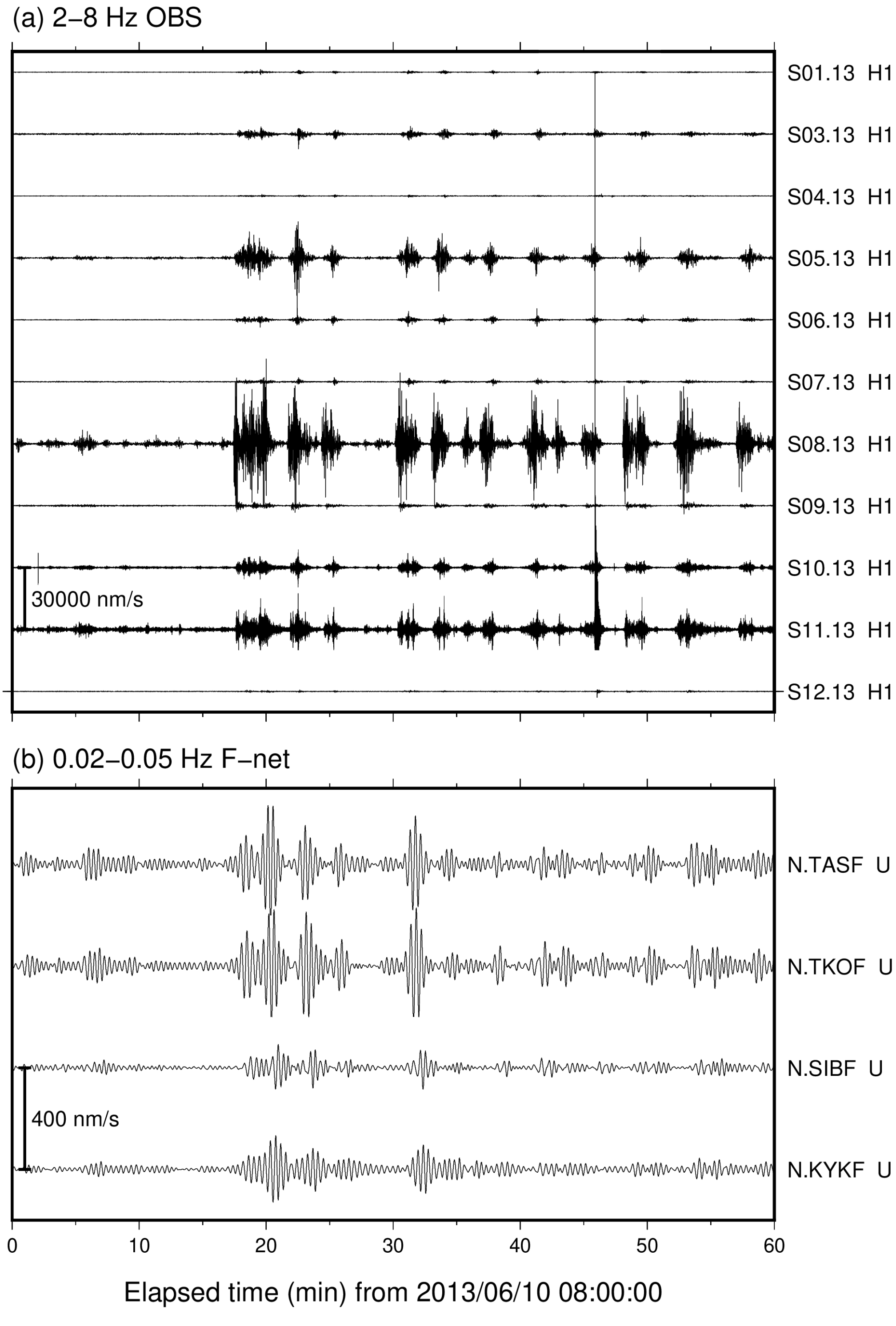

Fig.2. Example of one-hour records for (a) shallow tremors in a frequency range of 2–8 Hz at OBSs and (b) shallow VLFEs in a frequency range of 0.02–0.05 Hz at F-net stations.

2. Data and Method

2.1. Estimation of energy rate functions of tremors

For the analysis of tremors, we evaluated the energy rate functions of tremors located by Yamashita et al. (2015; 2021). We used 360 s broadband (NK1508 and NK1510 in 2015), 1 Hz (S06.13, S09.13 in 2013 and others in 2015) and 4.5 Hz (others in 2013) short-period OBS records of temporary seismological observations in Hyuga-nada. 11 and 12 stations were incorporated from April 17 to July 4, 2013 (Yamashita et al., 2015) and from January 1, 2015 to January 1, 2016 (Yamashita et al., 2021), respectively. The sampling rate was 200 Hz (S05.13, S06.13, S08.13, and S09.13 in 2013 and all OBSs in 2015) or 128 Hz (other OBSs in 2013). Analog seismic signals were digitized using a 16-, 20-, or 24-bit A/D converter. After instrumental responses were removed, a bandpass filter was applied in a frequency range of 2–8 Hz, and the vertical and horizontal components of the root-mean-square (RMS) velocity envelopes with a smoothing time window of 5 s were calculated. The envelopes were resampled at one sample per second. Examples of envelope waveforms of a tremor obtained by the RMS of the sums squared seismograms of two horizontal components are displayed in Fig. 3.

We estimated the site amplification factors of the vertical and horizontal components at each OBS relative to an F-net (Aoi et al., 2020) station, N.TASF, at 2–8 Hz and the quality factor of the *S*-wave attenuation (Q) by utilizing the information of the maximum *S*-wave amplitudes of intraslab regular earthquakes following the method of Yabe et al. (2019). The maximum *S*-wave amplitude of the i-th earthquake at the j-th station (A_{ij}) is expressed by the following relationship:

$$\ln(A_{ij}) = \ln(S_i) - \ln(\sqrt{4\pi}L_{ij}) - \frac{\pi f_c Q^{-1}}{V_S} L_{ij} + \ln(C_j) \quad (1)$$

where S_i is the size of the i-th seismic source, L_{ij} is the distance between the hypocenter of the i-th earthquake and the j-th station, f_c represents the central frequency (5 Hz in this study), V_s is the *S*-wave velocity (assuming 3.5 km/s in this study), and C_j is the site amplification factor. We measured the maximum *S*-wave amplitudes of regular earthquakes more than 5 km deeper than the plate boundary of the Japan Integrated Velocity Structure Model (JIVSM; Koketsu et al., 2012) with magnitudes larger than 2.5 listed in the regular earthquake catalog of the Japan Meteorological Agency (Fig. S1). We defined the maximum envelope amplitude of the time window from 2 s before to 50 s after the arrival time at each OBS as the maximum *S*-wave amplitude. The site amplification factor relative to N.TASF and Q^{-1} at each OBS was estimated by solving Equation (1) using the least-squares method. In the following procedures, we utilized the RMS of the sums of the squared three-component seismograms with a smoothing time window of 5 s after site correction by implementing the site amplification factors displayed in Fig. 4. After correcting the site amplification factors, the amplitudes were normalized by the site conditions at the reference onshore station, N.TASF. We also evaluated the average of Q^{-1} solved at each OBS in Equation (1) as $(3.4415 \pm 0.9585) \times 10^{-3}$. We adopted this value to estimate the energy rate functions of the tremors.

We calculated the energy rate functions of the tremors by implementing the site amplification factors and Q^{-1} estimated by the above procedures. The energy rate function of a tremor ($E_j(t)$), estimated from the amplitudes of the j-th station, was calculated using the following equation:

$$E_j(t) = 2\pi V_S r_j^2 \rho A''^2_j\left(t + t_j\right) \exp\left(2\pi f_c Q^{-1} t_j\right) \qquad (2)$$

where, $A''_j(t)$ is the amplitude of envelopes after the site-correction at the j-th station, r_j is the hypocentral distance from the tremor source to the j-th station, t_j is the travel time from the tremor source to the j-th station, and ρ is the density (assuming 2,700 kg/m^3 in this study). The epicentral locations of the tremors were set at those located by Yamashita et al. (2015, 2021). The depth of the tremors was set at the plate boundary of the JIVSM (Koketsu et al., 2012). To calculate the energy rate function, the time windows were set at 240 s, which started 60 s before the time window of the tremors set by Yamashita et al. (2015; 2021). We stacked the energy rate functions of a tremor for each station and estimated the average energy rate function $E_{\mathrm{ave}}(t)$ divided by the number of stations used. We calculated the cross-correlation coefficients (CCs) of the energy rate functions of all station pairs in Fig. 4 and further utilized the stations whose CCs exceeded 0.6 with at least one other station when stacking the energy rate functions.

The seismic energy W of a tremor is calculated by integrating $E_{\mathrm{ave}}(t)$ in the time range t_1–t_2:

$$W = \int_{t_1}^{t_2} E_{\mathrm{ave}}(t) dt. \qquad (3)$$

The integration range is the period when the values of $E_{ave}(t)$ exceed 20% of the maximum value of $E_{\mathrm{ave}}(t)$ (red line in the stacked energy rate function of Fig. 5). The duration of a tremor was defined as $t_2 - t_1$. The seismic energy rate of the tremor was estimated by dividing the seismic energy by the duration.

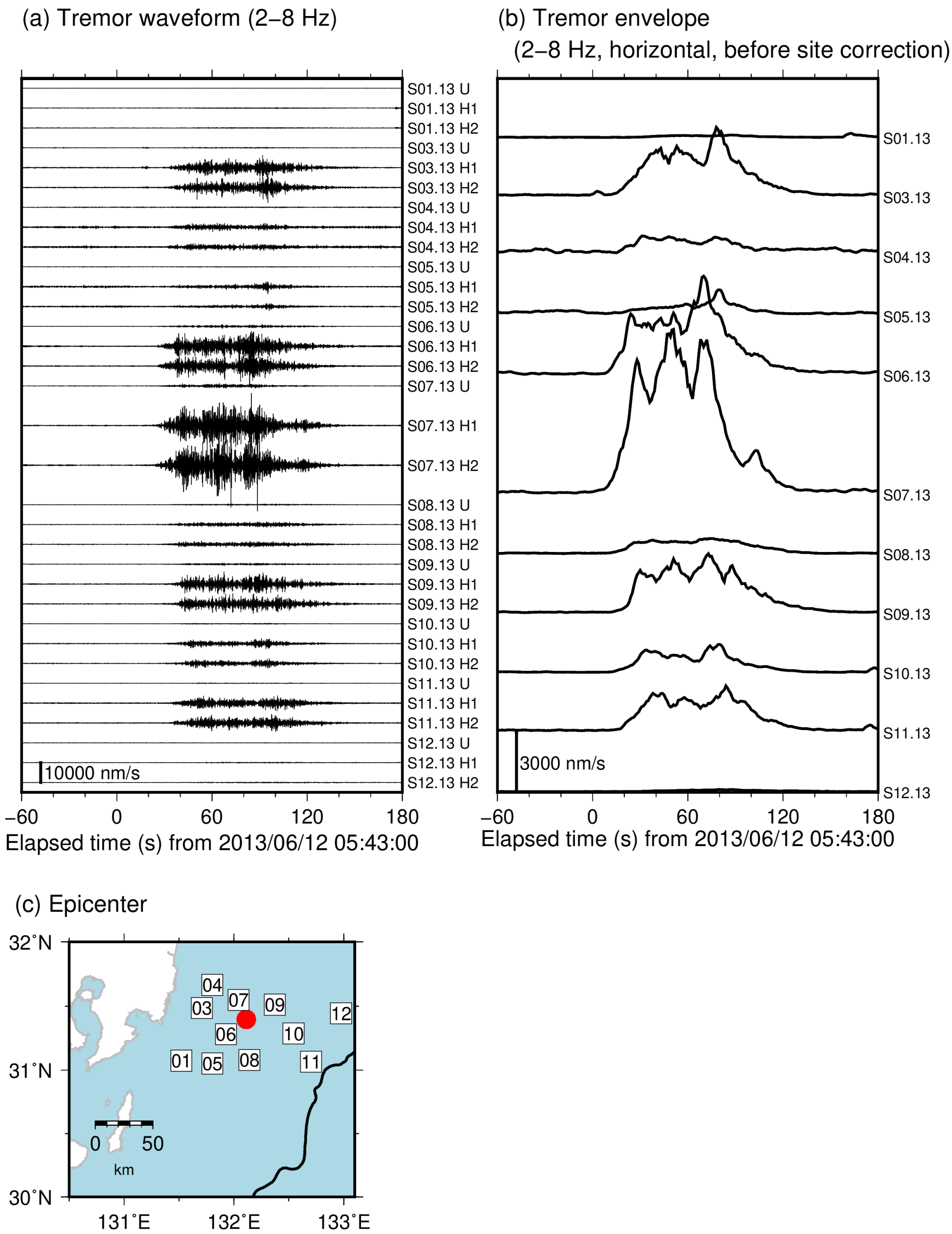

Fig. 3. Example of (a) waveforms of a tremor in a frequency range of 2–8 Hz, and (b) envelopes obtained by the root-mean-square of sums squared seismograms of two horizontal components. Waveforms are displayed from 05:43:00 (JST, UTC+9), June 12, 2013. (c) Red circle depicts the epicenter of the tremor as displayed in in Fig. 3a and b. Black line represents the trench axis. Squares indicate the locations of OBSs.

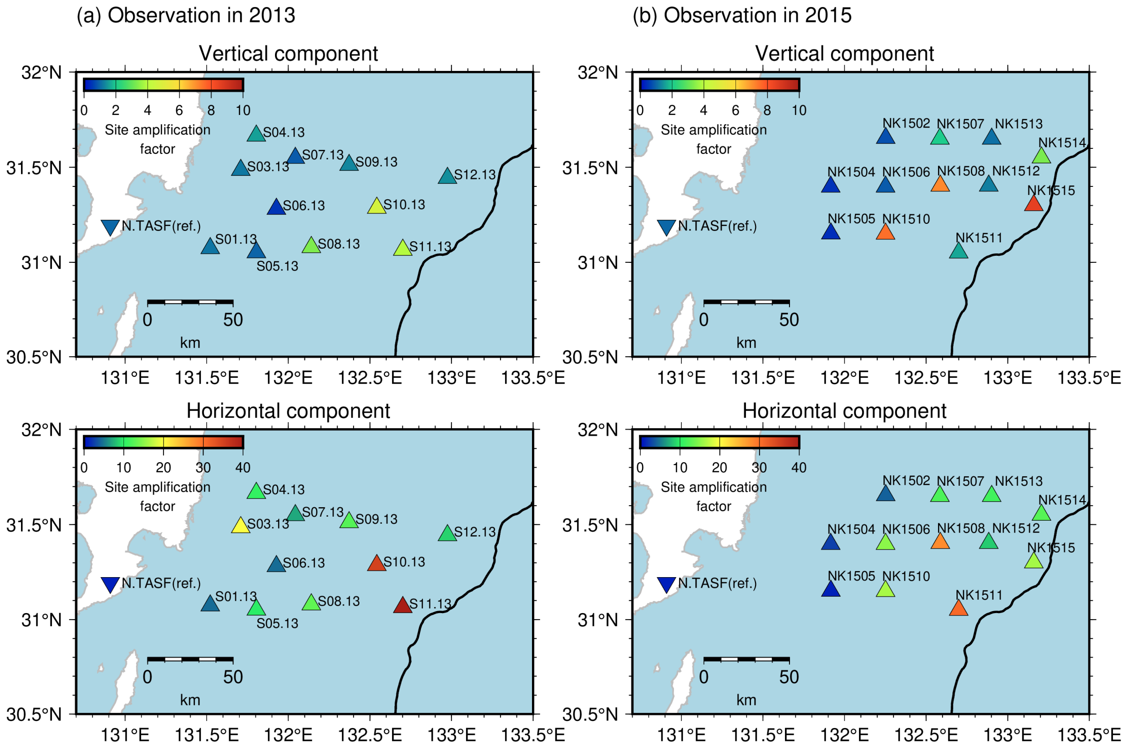

Fig. 4. Site amplification factors relative to N.TASF. Triangles represent the locations of OBSs. Inverted triangle indicates the location of the F-net station, N.TASF. Black line is the same as displayed in Fig. 3. Estimation error of site amplification factors is shown in Fig. S2.

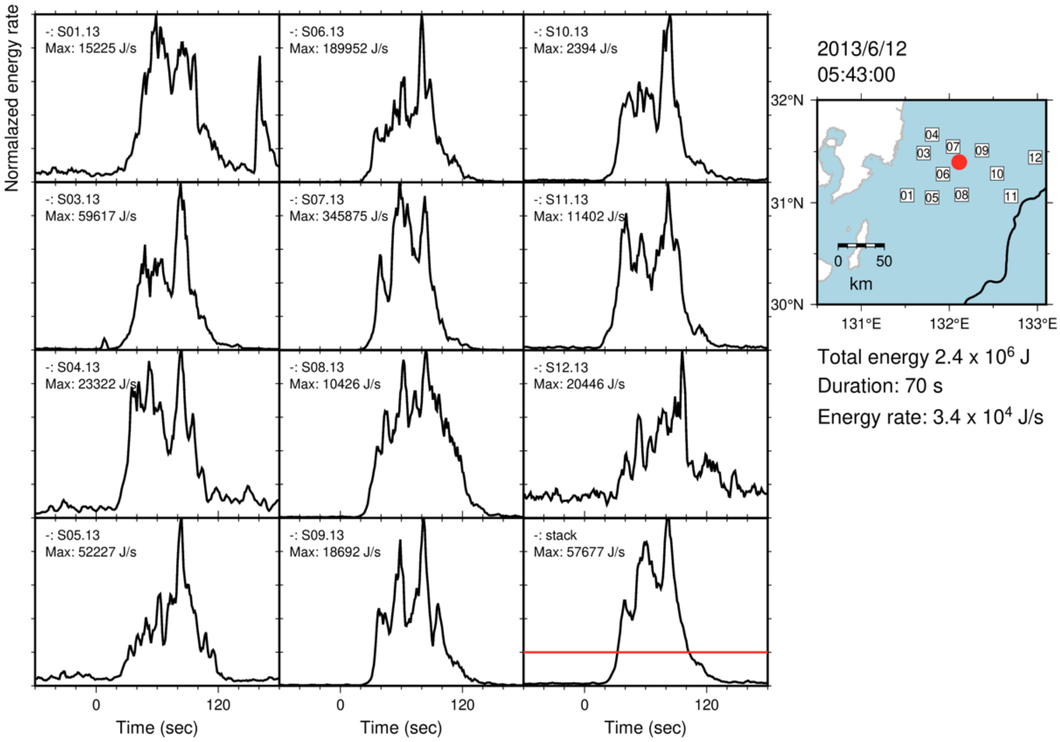

Fig. 5. Temporal changes of energy rate functions of a tremor estimated at each OBS along with its stacked energy rate function. Red line of the stacked energy rate function indicates the threshold, which is set as 20% of the maximum value of the energy rate function. Red circle, squares and black line are the same as displayed in Fig. 3.

2.2. Estimation of moments of VLFEs

We estimated the source durations and seismic moments of VLFEs temporally corresponding to the tremors in 2013 and 2015 detected by Yamshita et al. (2015; 2021) by comparing observed and synthetic waveforms following the procedure of Yabe et al. (2021) and Baba et al. (2021). We additionally estimated the source durations and seismic moments of VLFEs in 2010 detected by Asano et al. (2015) using the same method. As long-period VLFE signals are difficult to recognize in short-period OBS records, we utilized continuous seismograms at onshore broadband F-net stations for estimation. Before the analysis, we removed the instrumental responses, resampled at one sample per second, and applied a bandpass filter in a frequency range of 0.02–0.05 Hz to enhance the VLFE signals.

To reduce the computational costs of calculating Green's functions, reciprocal calculations were conducted using OpenSWPC (Maeda et al., 2017). We set source grids at an interval of 0.05° on the plate boundary of the area where tremors were detected (Fig. 6a). The hypocenter of each VLFE was supposed to be at the nearest grid from the hypocenter of the tremor located by Yamashita et al. (2015; 2021) or at the hypocenter of VLFEs located by Asano et al. (2015). JIVSM was implemented to calculate Green's functions. The minimum *S*-wave velocity in the elastic volume was set as 1.5 km/s. The model includes topography (ETOPO1; Amante and Eakins, 2009), air, and seawater layers. The default values of OpenSWPC were used for the density, seismic velocities, and quality factors in seawater and air. The model volume was discretized using a uniform grid of 0.2 km. The focal mechanisms were supposed to be consistent with the geometry of the plate boundary model of JIVSM and the plate convergence direction of the plate motion model NUVEL-1A (DeMets et al., 1994). By combining the assumed focal mechanisms and Green's functions, we prepared a series of synthetic velocity seismograms with triangular functions and source durations of 10–50 s (e.g., Takemura et al., 2019).

We calculated the station- and component-averaged CCs between the synthetic and observed waveforms in a time window of 150 s from the assumed origin time of a VLFE. The origin time was searched for in the range from 30 s before to 30 s after the start time of the duration range of the temporally corresponding tremor or the origin time of VLFEs located by Asano et al. (2015). The fit between the observed and simulated Love waves was not sufficient compared with the Rayleigh wave (Fig. 6b). It may be inferred that the sedimentary structure of JIVSM at very shallow depths (< 5 km) in Hyuga-nada is insufficient to simulate Love waves, which are sensitive to shallow structures. We verified that the CCs between the simulated and observed waveforms of a regular earthquake located by Takemura et al. (2020) in the transverse components were also low, whereas those in the vertical and radial components were high (Fig. S3). Therefore, we used only the vertical and radial components (Rayleigh waves) when calculating the CCs. For the N.KYKF station, only the vertical component was utilized because the horizontal components were noisy. The combination of source duration and origin time, with the highest average CC in the grid search, was adopted. We calculated the relative amplitudes by minimizing the variance reduction between simulated and observed waveforms (Baba et al., 2021; Yabe et al., 2021), and further estimated the seismic moments of VLFEs using the estimated relative amplitudes. The moment, duration, and average CC of the example in Fig. 6 were 2.0×10^{15} Nm, 24 s, and 0.65, respectively. Events with average CCs smaller than 0.3 were discarded. The seismic moment rate of the VLFE was obtained by dividing the seismic moment by the source duration.

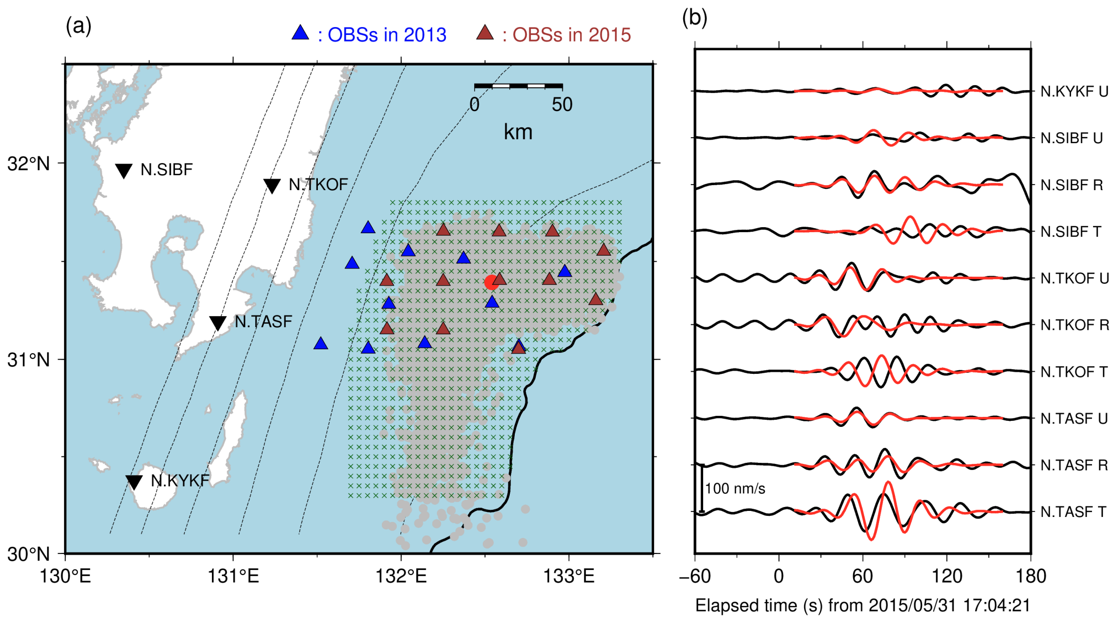

Fig.6. (a) VLFE source grids for the VLFE analysis. Green crosses indicate the locations of the VLFE source grids. Gray dots indicate the epicenters of tremors detected by Yamashita et al. (2015; 2021). Red circle indicates the epicenter of the event displayed in Fig. 6b. Blue and brown triangles depict the locations of OBSs in 2013 and 2015, respectively. Dashed contours indicate the isodepth of the top of the Philippine Sea plate at 10-km intervals (JIVSM; Koketsu et al., 2012). Black line represents the trench axis. Inverted triangles display the locations of the F-net stations. (b) An example of a VLFE in a frequency range of 0.02–0.05 Hz. Waveforms are depicted from 17:04:21 (JST, UTC+9), May 31, 2015. Black and red lines are the observed and the simulated waveforms, respectively. R, T, and U components represent the radial, transverse, and vertical components, respectively.

3. Results

We estimated the energies of 1,672 and 6,126 shallow tremors in 2013 and 2015, respectively. We classified the analysis region into three areas based on spatial variation in slow earthquake activity: Area A, south of 31.0º N; Area B, west of 132.3ºE, north of 31.0º N; and Area C, east of 132.3ºE, north of 31.0º N. In 2013, tremors and VLFEs occurred mainly in Areas A and B, whereas in 2015, they occurred mainly in Areas B and C. Area A is south of the subducted Kyushu-Palau Ridge, Area B is near the top of the subducted ridge, and Area C is east of the subducted ridge. Most of Areas A and C are outside the subducted ridge. The dominant range of tremor energies was 10^4–10^8 J with spatial variation (Fig. 7). In 2013 (Fig. 7a), tremors with large energies (> $10^{6.5}$ J) were concentrated in Area A. In 2015 (Fig. 7b), tremors with larger energies (> 10^7 J) occurred near the northeastern edge of the subducted Kyushu-Palau Ridge in Area C. The tremor energies near the trench axis in Area C were smaller.

The moments were also estimated for 1,297, 904, and 1,785 shallow VLFEs in 2010, 2013, and 2015, respectively. The dominant range of the VLFE moments was $10^{13.5}$–$10^{16.5}$ Nm (Fig. 8). South of 31.0º N (Area A), VLFEs with large moments (> $10^{15.5}$ Nm) occurred in 2010 and 2013 (Fig. 8ab). North of 31.0º N, VLFEs extended near the trench axis in 2010 and 2015. In particular, VLFEs with large moments (> $10^{15.5}$ Nm) in 2010 and 2015 (Figs. 8a and c) are concentrated east of 132.3º E (Area C). In the west of 132.3º E and north of 31.0º N (Area B), the VLFE moments are relatively small. The spatial variations in the VLFE moments and tremor energies for each observation period were similar (Figs. 7 and 8). The spatial variations in the energy rates of tremors and moment rates of VLFEs were also similar to those of tremor energies and VLFE moments (Figs. S4 and S5). The energies of the tremors and moments of VLFEs are generally larger outside the subducted ridge (Areas A and C) than near the top of the subducted ridge (Area B).

In the downdip of shallow tremors and VLFEs, repeating earthquakes occurred at depths of 15–30 km. The interplate slip rate estimated from repeating earthquakes was higher in the south along the strike direction (Fig. 9; Yamashita et al., 2012). The area with a large slip rate of repeating earthquakes is considered as weak interplate coupling; therefore, the interplate coupling may be weaker at depths of 15–30 km in the south (downdip part of Area A) than in the north (downdip of Area B). The cumulative moment of shallow VLFEs in 2010 and 2013, episodes with along-strike migrations, was also smaller in Area B than in Area A during the episodes (Fig. 9). By comparing the spatial variation in VLFE cumulative moments with the slip-deficit rate, Baba et al. (2020) found the tendency that cumulative moment of shallow VLFEs was larger in areas with weak interplate coupling along the Nankai Trough. In Hyuga-nada, the slip rate of repeating earthquakes and the cumulative moment of VLFEs are larger in the south (in and downdip of Area A) than in the north (in and downdip of Area B). These observations suggest that although there is a difference in the slip behavior along the dip direction, the along-strike variation in interplate coupling is consistent.

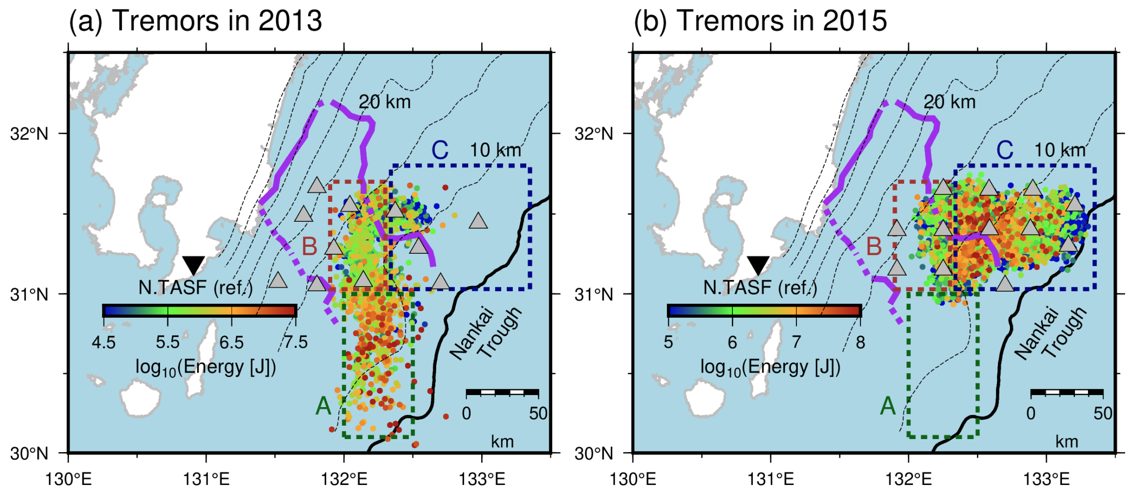

Fig. 7. Spatial distribution of energies of shallow tremors (a) in 2013 and (b) in 2015. Green, brown, and dark blue dotted rectangles indicate the ranges of Area A, B, and C, respectively. Purple lines represent the inferred subducted Kyushu-Palau Ridge (Yamamoto et al., 2013). Gray triangles depict the locations of OBSs. Inverted triangles and black line are the same as displayed in Fig. 3. Dashed contours indicate the isodepth at the top of the Philippine Sea plate in intervals of 5 km (Nakanishi et al., 2018).

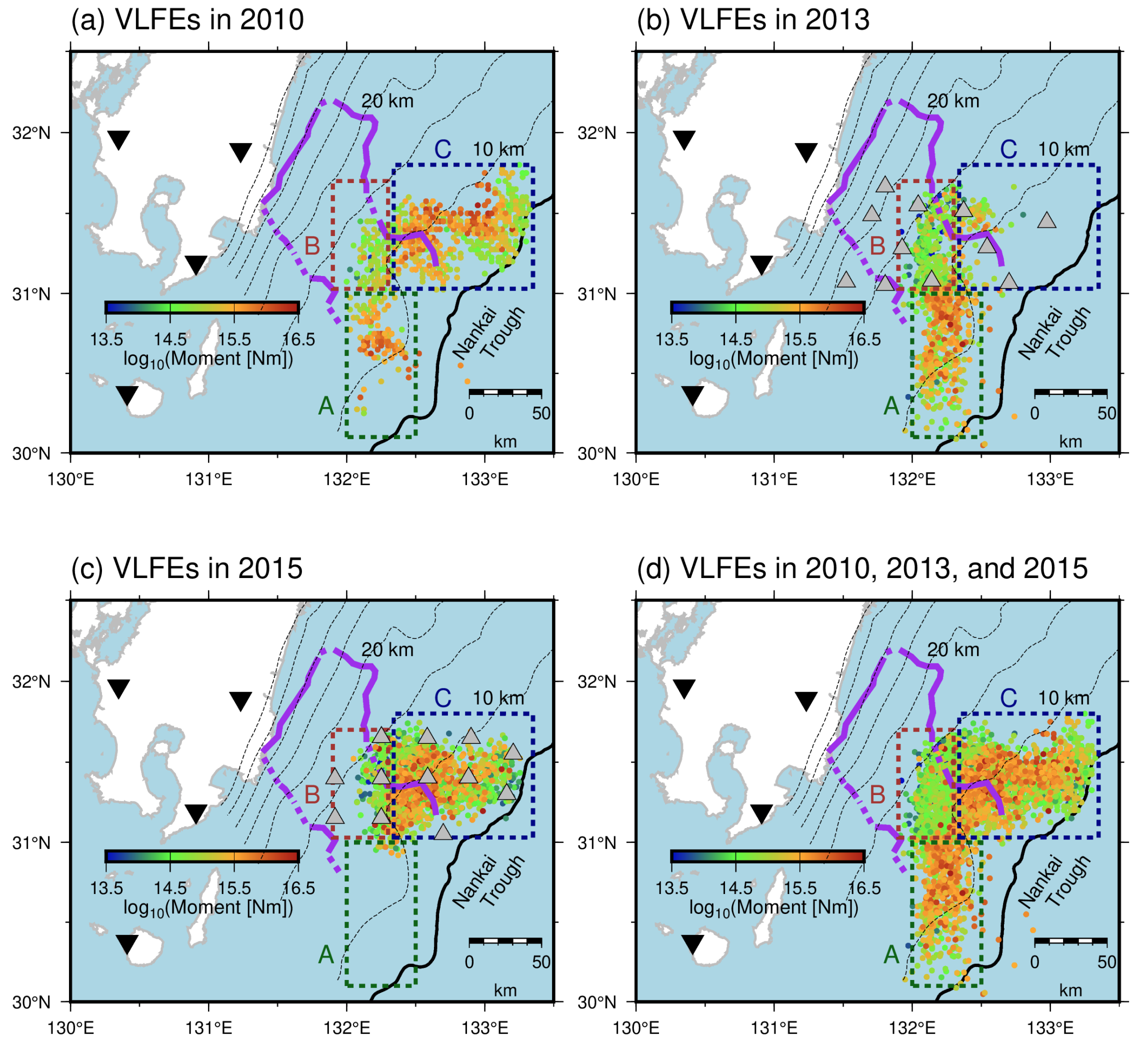

Fig. 8. Spatial distribution of moments of shallow VLFEs in (a) 2010, (b) 2013, (c) 2015, and (d) all analysis periods. Colored dotted rectangles, dashed contours, purple lines, black line and gray triangles are the same as displayed in Fig. 7.

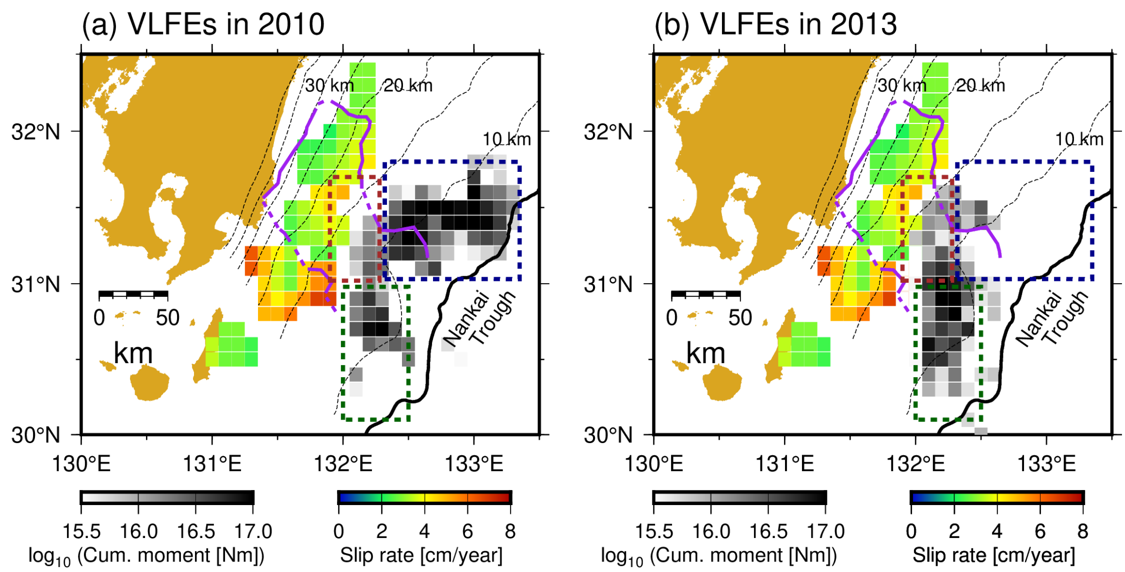

Fig. 9. Relationship between slip rates estimated from repeating earthquakes (Yamashita et al., 2012) and shallow slow earthquakes. Gray scales exhibit the cumulative moments of VLFEs. Color scale indicates the slip rate estimated from repeating earthquakes. Colored dotted rectangles, purple lines, black lines, and dashed contours are the same as in Fig. 8.

4. Discussion

4.1 Spatial variation in slow earthquake activity along the strike direction

In Sections 4.1 and 4.2, we focus on the along-strike migrations in 2010 and 2013, because the spatial variation in moments and energies of slow earthquakes and the change in migration speed are associated (Fig. 10a and b). We mainly discuss the spatial variation based on VLFE activity because the spatial variations in VLFE moments and tremor energies were similar, and the VLFE analysis covered all episodes in 2010, 2013, and 2015. Migrations along the strike direction in 2010 and 2013 consistently started south of the subducted Kyushu-Palau Ridge (Area A). Subsequently, the VLFEs migrated northward and entered the subducted ridge. After VLFEs entered Area B, their migration speed became slow, and the moments of the VLFEs were small (Fig. 10a and b). The spatiotemporal variation in the migration front seems to be parabolic (discussed in detail in Section 4.2). As indicated by Yamashita et al. (2015), rapid tremor reversals (RTRs; black dotted arrows in Figs. 10b and S6d), which is a fast backward migration (e.g., Houston et al., 2011), occurred during the migration in 2013. When RTRs entered Area A, the moments of the VLFEs become large; therefore, the moments depend on the area.

We divided each episode in 2010 and 2015 into three migrations and the 2013 episode into two migrations. The 2010a, 2013a, and 2013b migrations were along the strike direction, whereas the 2010b, 2010c, 2015a, 2015b, and 2015c migrations were along the dip direction (Figs. 10a and S6; Table S1). The along-strike migrations were always northward (Figs. 10b, S6a, S6d, and S6e) (Yamashita et al., 2015), whereas there were various directions for the along-dip migrations. The 2010b, 2015a, and 2015b migrations were eastward (Figs. 10c, S6b, S6f, and S6g) (Yamashita et al., 2021), whereas the 2010c migration was westward (Figs. S6h). The 2015c migration was bilateral (Fig. S6c).

The spatial changes in deep slow earthquake activity in Shikoku are similar to those in Hyuga-nada. The energy of tremors is larger, the along-strike migration speed is faster, and the number of tremors is smaller in western Shikoku than in central Shikoku (Table 1; Kano et al., 2018b). In Hyuga-nada, the migration speed was faster (Fig.10b) and the average moment of VLFEs was larger in Area A than in Area B (Fig.11); therefore, the migration speed and VLFE moment have a positive correlation as with tremor activity in Shikoku. In addition, the number density of events was larger in Area B than in Area A in Hyuga-nada (Fig. 12). From the viewpoint of migration speed, tremor energy or VLFE moment distribution, and number density, the relationship between western and central Shikoku corresponds to that between Area A and Area B in Hyuga-nada, respectively. A similar relationship was also found in shallow VLFE activity around the subducted Paleo-Zenisu Ridge off the southeast Kii Peninsula (Yamamoto et al., 2022). The relationship between the west of and inside the subducted Paleo-Zenisu ridge in this region corresponds to that between Area A and Area B in Hyuga-nada. We discuss spatial variation based on the physical models in Section 4.2.

In western Shikoku, the pore fluid pressure at the plate boundary is suggested to be lower than that in central Shikoku (Kano et al., 2018b; Table 1). The pore fluid pressure at the plate boundary can affect the frictional properties of the faults. Therefore, we compared the *P*-wave velocity structure investigated in Nishizawa et al. (2009; Fig. 11a) and the cumulative moment at each grid of 10 km × 10 km along the structure profile (Fig. 11b). The average moment of VLFEs was small and large in Area B (at a distance of 0–30 km) and in Area A (at a distance of 30–60 km), respectively, along the profile (Fig. 11b). There is a low seismic velocity anomaly in Area A (Fig. 11a). The low velocity anomalies can be a result of the high pore fluid pressure around the plate boundary; therefore, the spatial variation in the slow earthquake activity between Areas A and B may be related to the existence of the low velocity anomaly. This is discussed in more detail in Section 4.2.

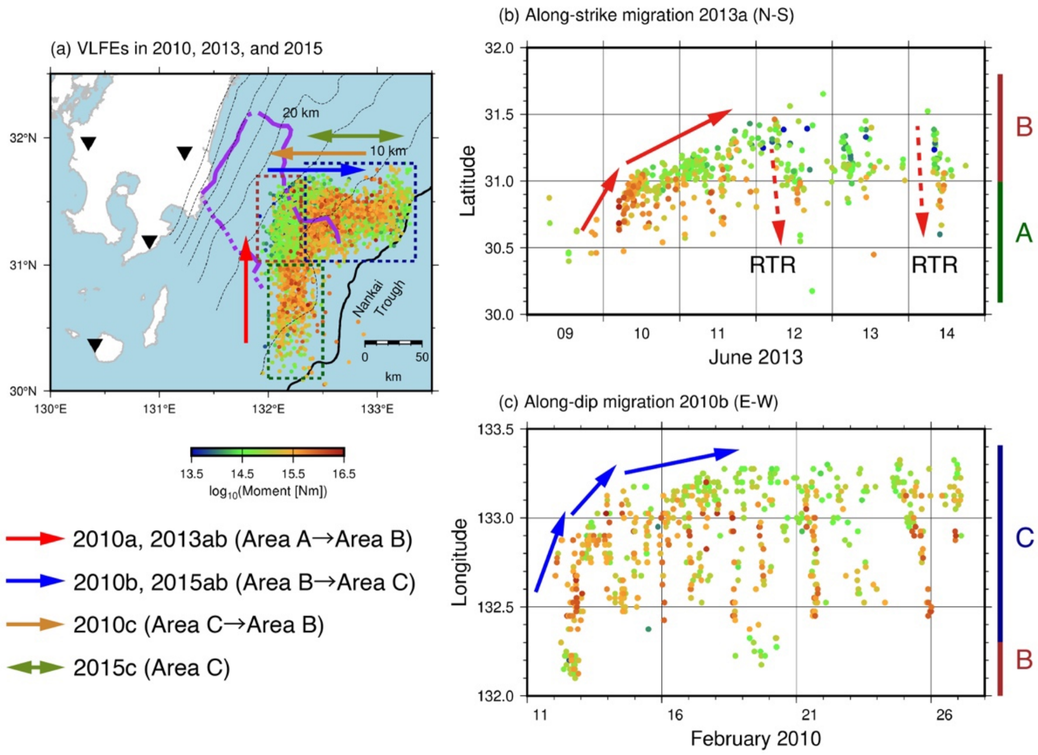

Fig. 10. (a) Summary of slow earthquake migration patterns. Colored arrows represent the direction of migration patterns. Colored dotted rectangles, dashed contours, purple lines and black inverted triangles are the same as displayed in Fig. 8. (b) Spatiotemporal distributions of (b) an along-strike migration 2013a and (c) along-dip migration 2010b with moments of VLFEs. Black arrows indicate the direction of migrations. Black dotted arrows in Fig. 9b represents the RTR.

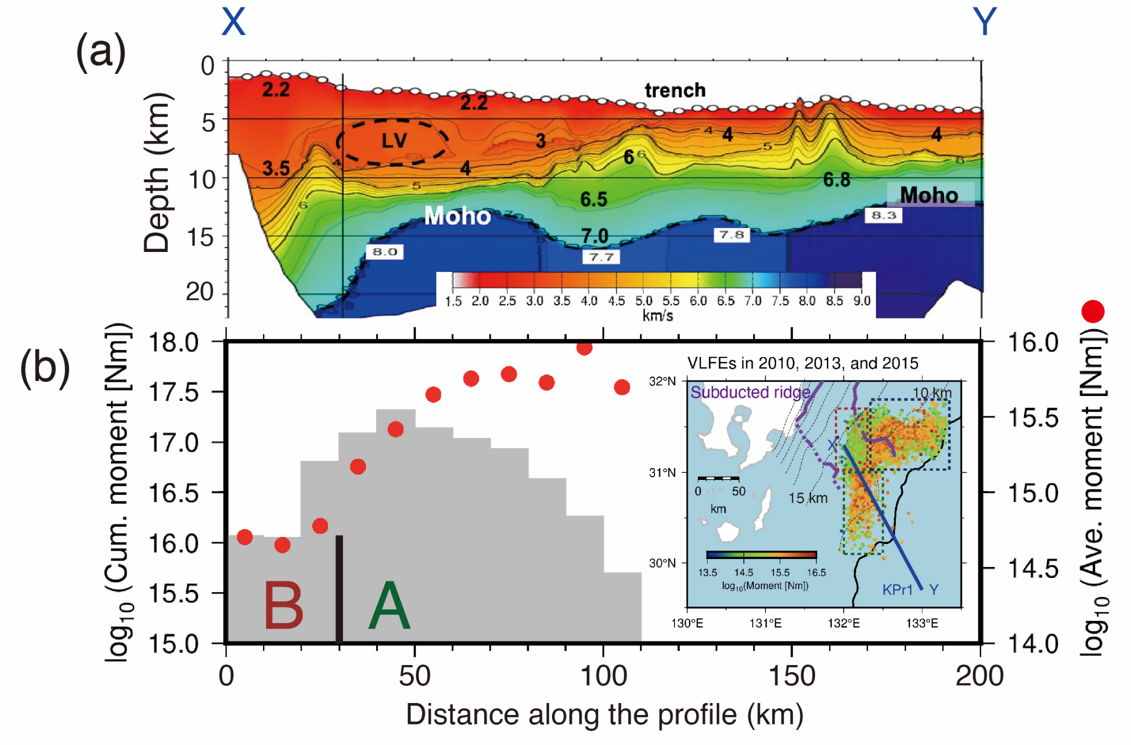

Fig. 11. (a) *P*-wave structure model along the profile (Nishizawa et al., 2009) and (b) histogram of cumulative moment and average moment of VLFEs at each grid of 10 km × 10 km in the horizontal directions. Grids are set along the profile and the profile penetrates the center of the ordered grids. The red circles in Fig. 11b display the average moment of VLFEs at each grid. The profile is indicated by a blue line in the map in Fig. 11b. Colored dotted rectangles, purple contour, black line, and dashed contours in the map are the same as displayed in Fig. 8.

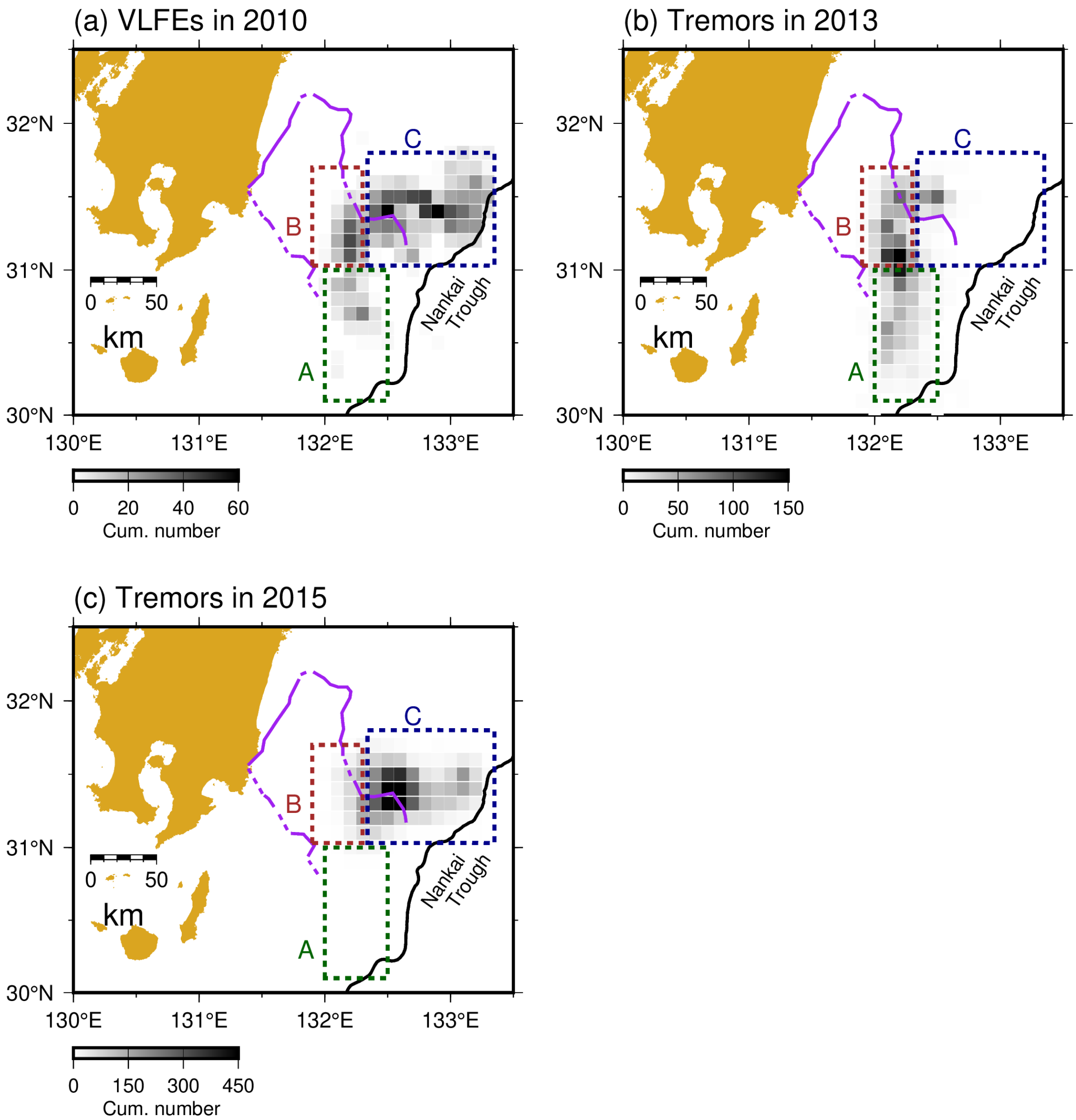

Fig. 12. Event number distribution in the grid of 1° × 1°. (a), VLFEs located by Asano et al. (2015), (b), tremors located by Yamashita et al. (2015), (c), tremors located by Yamashita et al. (2021). Colored dotted rectangles, purple lines, and black lines are the same as in Fig. 8.

Table 1. Variation in slow earthquake activity in Hyuga-nada and in Shikoku (Kano et al., 2018b). Checkmarks in the table represent that the characteristic of slow earthquake activity or fault condition on the plate boundary in Shikoku is also observed in Hyuga-nada. The pore fluid pressure on the plate boundary in Hyuga-nada is interpreted from the seismic velocity structure investigated by Nishizawa et al. (2009). Tidal sensitivity of slow earthquakes in Hyuga-nada was indicated by Katakami et al. (2017).

This study (Hyuga-nada) Kano et al. (2018; Shikoku)	Area A Western Shikoku	Area B Central Shikoku	Observation in Hyuga-nada
Migration speed	Fast	Slow	✓
Energy or moment	Large	Small	✓
Pore fluid pressure on the plate boundary	Low	High	✓?
Tidal sensitivity	Low	High	✓
Number of events	Small	Large	✓
Interpretation	Strong patch area	Weak patch area	

4.2. Spatial variation in rupture process inferred from physical models

To investigate the controlling factor of the along-strike variation in slow earthquake activity in Hyuga-nada, we compared the activity with a physical model of along-strike slow earthquake migration by Ando et al. (2012). They predicted that ETS starts migrating energetically in strong patch areas and decelerates with a parabolic spatiotemporal pattern in weak patch areas. In their model, strong and weak brittle patches exist on the ductile background based on Newtonian rheology. In Hyuga-nada, the migration speed was faster, and the VLFE moment was larger in Area A than in Area B. These observations are consistent with the model by Ando et al. (2012). The along-strike variation in slow earthquake activity in Hyuga-nada can be explained by the difference in the patch strength of slow earthquakes, where Areas A and B are considered strong and weak patch areas, respectively (Fig. 13).

The spatial variations in slow earthquake activity in Shikoku and off the southeastern Kii Peninsula were also discussed based on Ando et al. (2012) (Shikoku: Kano et al., 2018b; off the southeast Kii Peninsula: Yamamoto et al., 2022). In Shikoku, western and central Shikoku are interpreted as strong and weak patch areas, respectively, whereas the areas west of and inside the subducted Paleo-Zenisu ridge off the Kii Peninsula are regarded as strong and weak patch areas, respectively.

As mentioned in Section 4.1, there is a low velocity anomaly in Area A (Fig. 11a). The existence of low velocity anomalies can be considered a result of the high pore fluid pressure around the plate boundary. We interpreted that a low velocity anomaly in Area A exists in the hanging wall. Based on the similarity with slow earthquake activity in Shikoku (Kano et al., 2018b), the fluid pressure on the plate boundary may be lower and the effective normal stress is higher in Area A than in Area B; therefore, the patch strength may be stronger in Area A than in Area B (Fig. 13). Hydrological or material properties along the slow earthquake faults may vary between Areas A and B. To discuss the variation in these properties in Hyuga-nada in more detail, investigations of seismic velocity structures (especially V_S and V_P/V_S ratio) are required in future work. Katakami et al. (2017) suggested that the correlation between tremor activity and tides was low at the start of the 2013 tremor migration in Area A, whereas tremor activity was sensitive to the tidal changes in the latter part of the tremor migration in Area B in Hyuga-nada. Therefore, tidal sensitivity was considered to be higher in Area B (weak patch area) than in Area A (strong patch area). This characteristic is similar to that of the deep tremor activity observed in Shikoku (Table 1). It is suggested that weak slow earthquake patches are easily ruptured by external stress perturbations, such as tidal changes (Kano et al., 2018b).

As mentioned in Section 4.1., the spatiotemporal variation in the migration front appears to be parabolic. Following Ando et al. (2012), we investigated which function is better for fitting the migration front in 2013a, exponential ($t=C\exp(x)$; t is the elapsed time, x is the migration distance, and C is constant) or parabolic ($t=D^{-1}x^2$; D is the diffusion coefficient). Although tremor epicenters were scattered around the start of migration, the migration pattern seems to be better fitted by a parabola (Fig. 14), and the diffusion coefficient D is evaluated as ~6×10^4 m^2/s. The relationship between D and the velocity strength coefficient η_v, is described by Ando et al. (2012):

$$\eta_v = \frac{\mu L}{2\pi D}\frac{\Delta\tau}{\tau_e} \quad (4)$$

where μ is the rigidity, L is the width of the strong patch, and $\Delta\tau/\tau_e$ is the stress drop normalized by the strength excess. In the observations in Hyuga-nada, the D and L of shallow slow earthquakes are ~6×10^4 m^2/s and ~8×10^4 m, respectively. Although these values are larger than those of deep tremor activity in the Kii Peninsula evaluated by Ando et al. (2012) (D~0.5×10^4 m^2/s and L~10^4 m), if μ and $\Delta\tau/\tau_e$ are the same as in the Kii Peninsula, the value of η_v is evaluated as ~10^{10} Pa s m^{-1}, which is similar to that estimated by Ando et al. (2012) on the order scale.

The patch strength in Ando et al. (2012) is represented by the amount of stress drop. Therefore, we evaluated the variation in the stress drop of the VLFEs in Hyuga-nada. Assuming a circular crack model, the seismic moment M_0 of an earthquake is given by (e.g., Kanamori and Anderson, 1975):

$$M_0 = \frac{16}{7}\Delta\tau r^3 \quad (5)$$

where $\Delta\tau$ is the stress drop and r is the radius of the patch. In this section, this relationship is further assumed in VLFEs. The average moment of a VLFE in Area A (strong patch area) and in Area B (weak patch area) is 2.4×10^{15} Nm and 5.6×10^{14} Nm, respectively (Fig. 11b). If constant patches with a radius r of 5 km are assumed (e.g., Ohta and Ide, 2017), the average stress drop of a VLFE in Areas A and B is evaluated as 8×10^{3} Pa and 2×10^{3} Pa, respectively. The spatiotemporal distribution of migration is parabolic if the difference in stress drop between strong and weak patches is sufficient (Ando et al., 2012). As indicated by the fitting of the migration front, the spatiotemporal variation in the slow earthquake migration front was parabolic (Fig. 10b). Although the model of Ando et al. (2012) assumed an 11-times differences between strong and weak patches, a parabolic migration pattern was observed by an approximately four-time difference in the stress drops of these patches in Hyuga-nada.

Based on the rate- and state-dependent friction laws, the rupture propagation speed is negatively correlated with the ratio of the length of the velocity-weakening materials to the total length (η) (Skarbek et al., 2012). We consider that the tremor migration speed corresponds to the rupture propagation speed of the SSE (e.g., Bartlow et al., 2011); therefore, we discuss based on this assumption. In Hyuga-nada, the migration speed, which corresponds to the rupture velocity of a shallow SSE, was faster in Area A than in Area B (Fig. 10b). According to their results, the value of η may be larger in Area A than in Area B. Skarbek et al. (2012) suggested that the migration speed and stress drop are negatively correlated with a/b (a and b are frictional parameters of the rate- and state-dependent friction law) in velocity-weakening areas (i.e., $a/b < 1$) if η is constant. As described above, the stress drop of VLFEs may be larger in Area A; therefore, the absolute value of a-b in a velocity-weakening material may be larger in Area A. The heterogeneity of slow earthquake activity may be controlled by frictional factors, such as η or a-b.

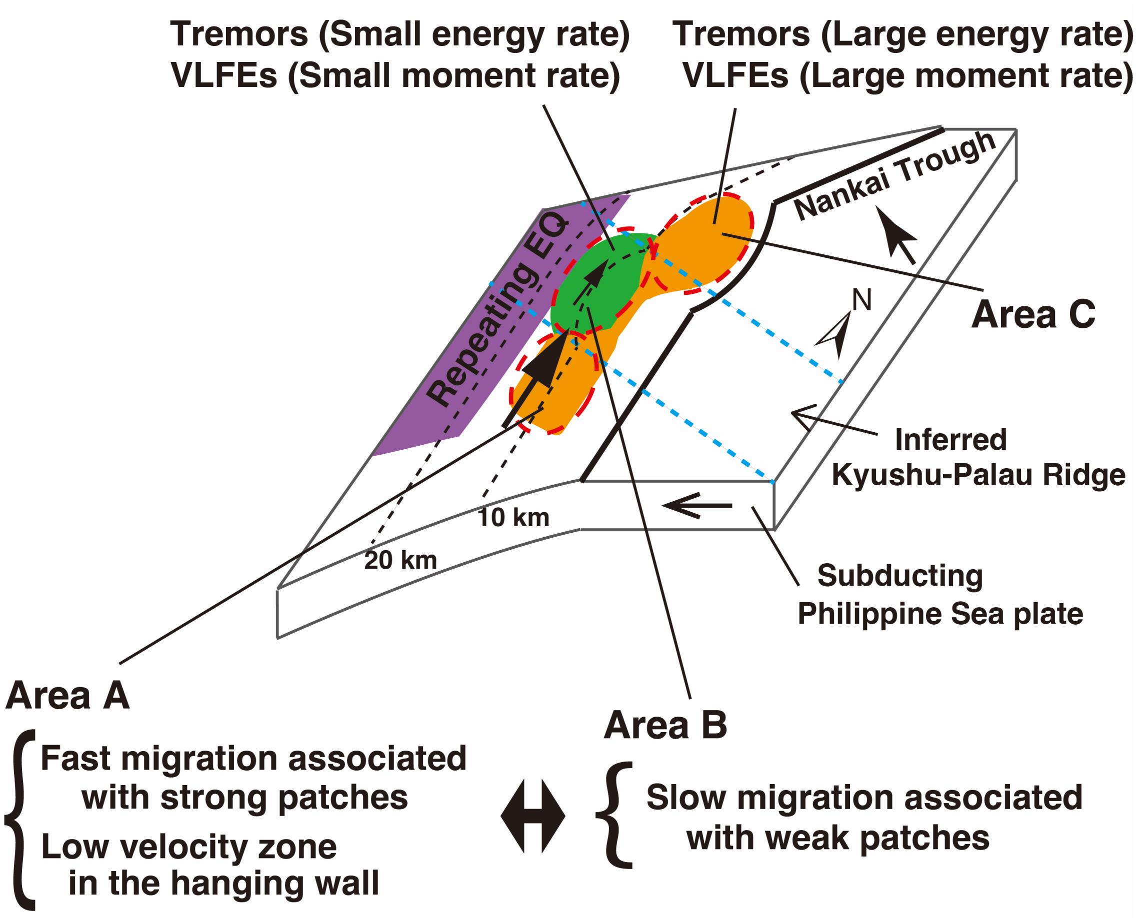

Fig. 13. Schematic illustration of the interpretation of distributions of slow earthquakes and Kyushu-Palau Ridge.

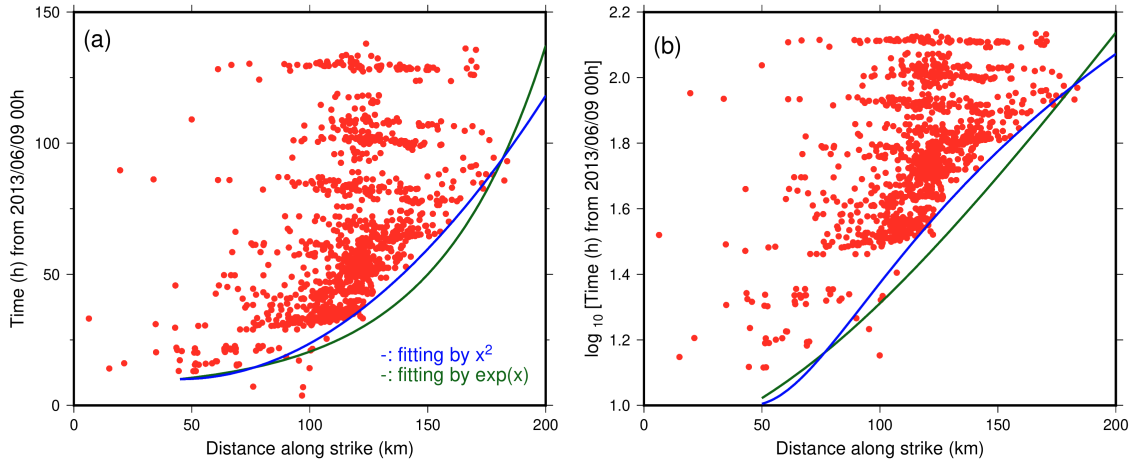

Fig. 14. (a) Spatiotemporal distribution of tremor migration in the episode of 2013a. Vertical and horizontal axis shows the elapsed time from 2013/06/09 00:00:00 JST, and Distance along the strike (N-S) from 30.0ºN, respectively. Blue and green lines indicate the parabolic and exponential curves, respectively. (b) Same as (a) but the vertical axis is log-scale.

4.3. Scaled energy of shallow slow earthquakes in Hyuga-nada

Recently, slow earthquake signals have been also detected in the microseism frequency band between tremors and VLFEs (Kaneko et al., 2018; Masuda et al., 2020; Yamashita et al., 2021); therefore, slow earthquakes are supposed to be broadband phenomena. To investigate the characteristics of broadband slow earthquakes, we evaluated the scaled energy of the slow earthquakes in Hyuga-nada. We estimated the scaled energy using the ratio between the seismic energy rate of a tremor and the seismic moment rate of the accompanying VLFE for activities in 2013 and 2015, in which the energy rate could be estimated from the OBS records. The dominant range of the scaled energy was 10^{-11}–10^{-8} both in 2013 and 2015 (Fig. 15ab). Although the distribution of the median scaled energy is smaller around the eastern edge of the Kyushu-Palau Ridge in Area C, the range of the median scaled energy is in the range of 10^{-10}–10^{-9} in all areas (Fig. 15cd); therefore, the spatial variation in the median scaled energy is similar in the order scale.

The scaled energy of shallow slow earthquakes in Hyuga-nada is 10^{-11}–10^{-8}, which is scattered compared to those in other regions along the Nankai Trough except Hyuga-nada (10^{-10}–10^{-8}; Yabe et al., 2021, 2019), along the Japan Trench (10^{-10}–10^{-9}; Yabe et al., 2021), and in Costa Rica (10^{-9}–10^{-8}; Baba et al., 2021), or that of deep slow earthquakes in southwest Japan, Cascadia, and Mexico ($10^{-9.5}$–10^{-9}; Ide, 2016; Ide and Maury, 2018; Ide and Yabe, 2014; Fig. 16). The reason for the broad range of scaled energies in Hyuga-nada can be that the dominant range of moment rates of shallow VLFEs here extends to 10^{15} Nm/s, which is one order larger than that of other shallow slow earthquake regions (10^{12}–10^{14} Nm/s; Nakano et al., 2018; Takemura et al., 2019; Yabe et al., 2021). Hyuga-nada can also be characterized from the perspective of the scaled energy of slow earthquakes. Similar dominant ranges of scaled energies in 2013 and 2015 (Fig. S7) suggest that the scaled energy did not change temporally.

Ide (2008) and Ide and Maury (2018) evaluated the characteristic time α^{-1} of seismic slow earthquakes in deep southwest Japan, Cascadia, and Mexico as 0.3–30 s. The range of α^{-1} of the SSE scale in deep southwest Japan, Cascadia, and Mexico evaluated by Ide and Maury (2018) is 75–300 s. α^{-1} is inversely proportional to the ratio of the long-term averages of energy rates to the square of the long-term averages of moment rates; thus, α^{-1} in Hyuga-nada is estimated to be 3–10000 s. In Hyuga-nada, there may be slow earthquake events that have similar or longer characteristic times than those of other slow earthquake regions. In addition, the range of the characteristic time is broader in Hyuga-nada than in other slow earthquake regions; therefore, slow earthquakes in Hyuga-nada may have various spectral features.

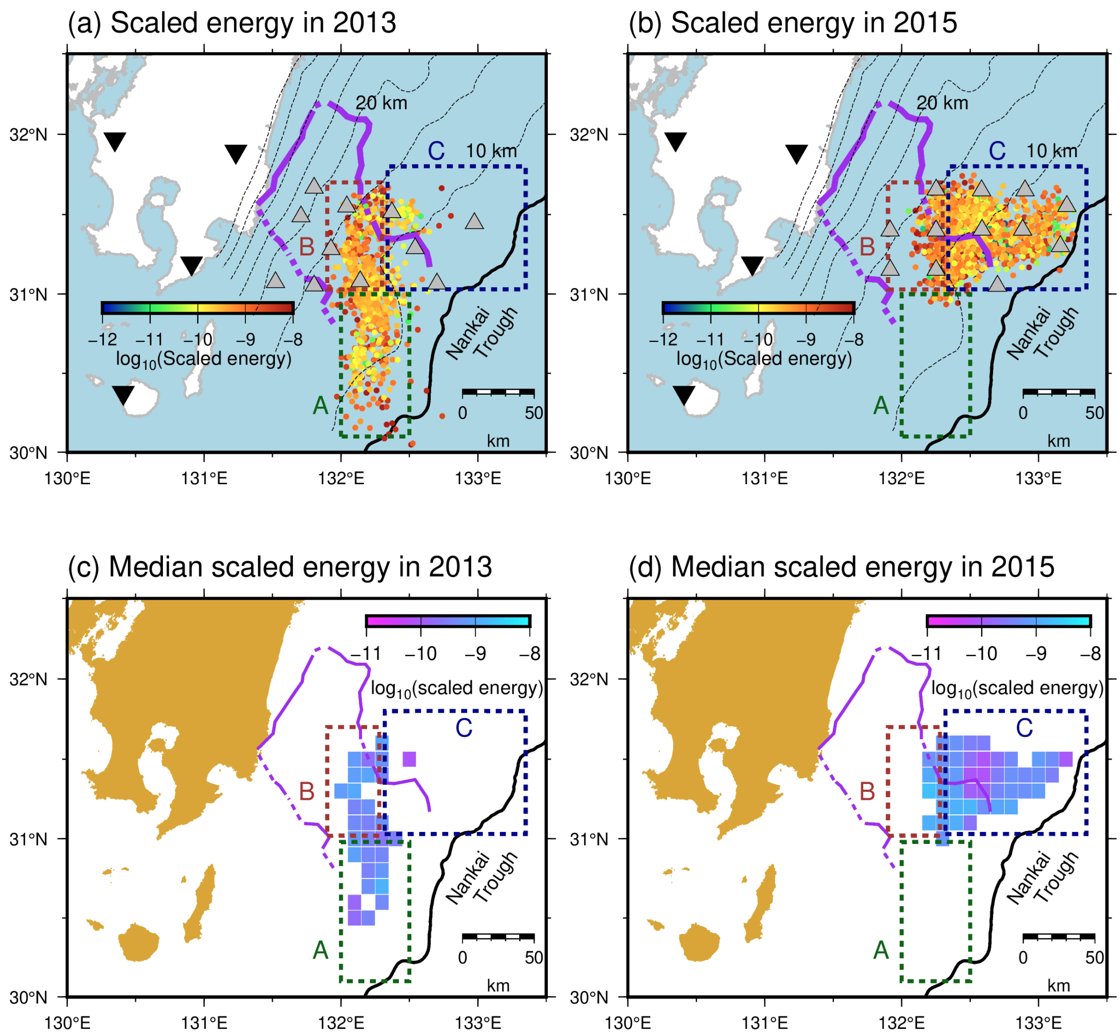

Fig. 15. Spatial distribution of scaled energy of shallow slow earthquakes (a) in 2013 and (b) in 2015. Spatial distribution of the median scaled energy in the grid of 1° × 1° where the number of event is larger than 10 (a) in 2013 and (b) in 2015. Colored dotted rectangles, purple lines, black lines, fray triangles, inverted triangles, and dashed contours are the same as in Fig. 8.

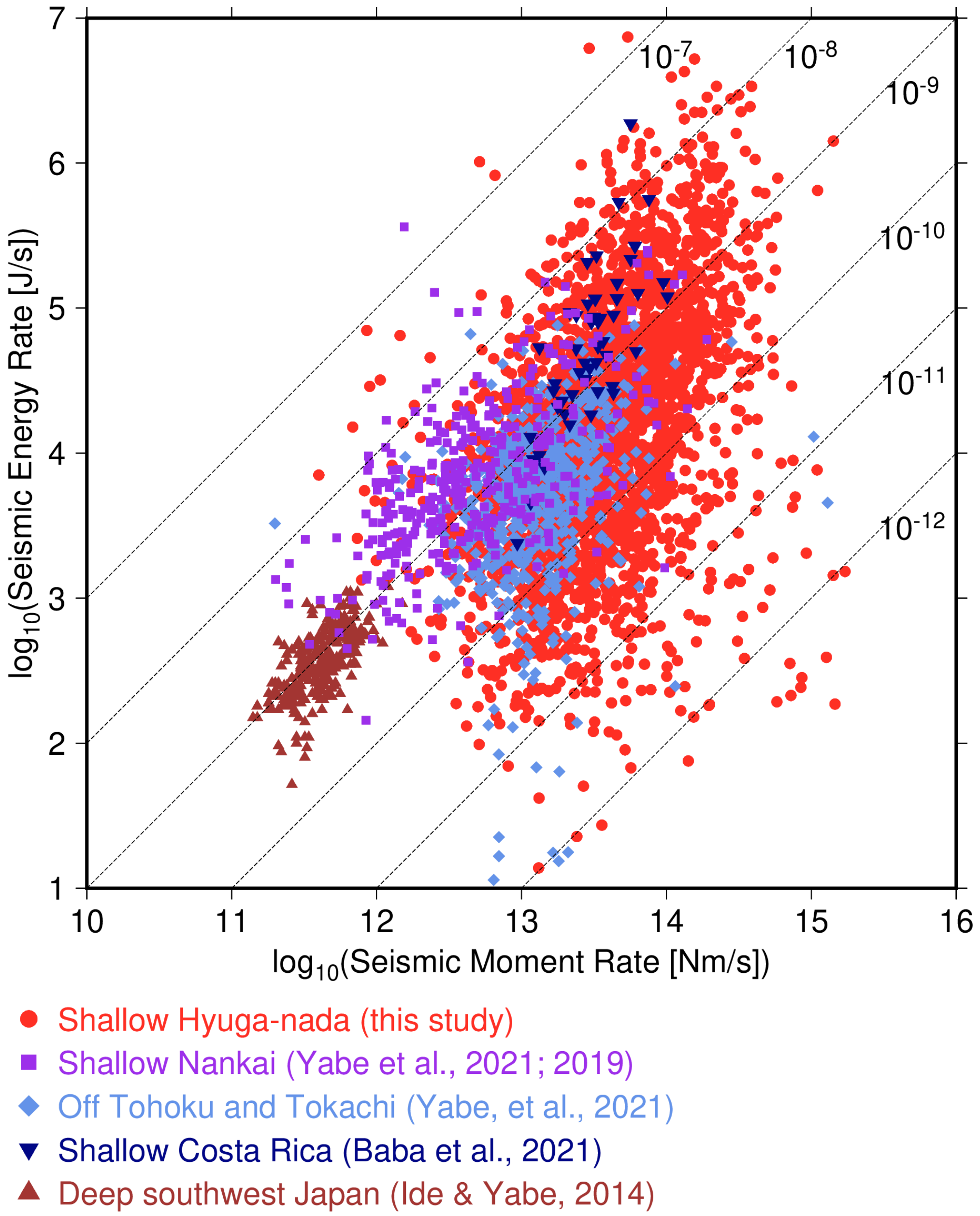

Fig. 16. Relationship between seismic moment rates of VLFEs and seismic moment rates of tremors. Red circles, purple squares, green diamonds, dark blue inverted triangles, and dark blue triangles indicate the relationships between seismic moment rates of VLFEs and seismic moment rates of tremors in shallow Hyuga-nada (this study), shallow Nankai except Hyuga-nada (Yabe et al., 2021, 2019), off Tohoku and Tokachi (Yabe et al., 2021), shallow Costa Rica (Baba et al., 2021), and deep slow earthquakes (Ide, 2016; Ide and Maury, 2018; Ide and Yabe, 2014). Dashed lines represent scaled energies of 10^{-7}, 10^{-8}, 10^{-9}, 10^{-10}, 10^{-11}, and 10^{-12}.

5. Conclusion

To investigate the spatial variation in the source characteristics of shallow slow earthquakes in Hyuga-nada at a higher resolution, we estimated the energies of shallow tremors, moments of shallow VLFEs, and the scaled energy of shallow slow earthquakes in Hyuga-nada using the data from permanent onshore broadband and temporary offshore seismometers. The dominant ranges of energies of tremors and moments of VLFEs are 10^4–10^8 J and $10^{13.5}$–$10^{16.5}$ Nm/s, respectively. The energies of tremors and moments of VLFEs are larger in Areas A and C (most of which are outside the subducted Kyushu-Palau Ridge) than in Area B (near the top of the subducted ridge). The migration of tremors and VLFEs along the strike direction started in Area A (south of the subducted ridge) with events of larger energies and moments. After going north and entering Area B (near the top of the subducted ridge), the migration speed slowed, and the energies of tremors and moments of VLFEs were observed to be small (Fig. 9b).

Based on the physical model of Ando et al. (2012), Areas A and B correspond to the strong and weak patch areas, respectively. The spatiotemporal distribution of the tremor migration in 2013 is fitted by a parabolic function. If a circular crack model is assumed, the average stress drop of the VLFEs in Area A (strong patch) and Area B (weak patch) are evaluated as 8×10^3 Pa and 2×10^3 Pa, respectively. An approximately four times difference in the stress drop of strong and weak patches can generate a parabolic migration pattern. The along-strike variation in the rupture process on the plate boundary, such as the stress drop, in slow earthquake regions can cause variations in the moment of slow earthquakes and migration pattern near the southern edge of the subducted ridge.

Data Availability

A part of OBS data for this study was acquired by "Research project for compound disaster mitigation on the great earthquakes and tsunamis around the Nankai Trough region," a project of the Ministry of Education, Culture, Sports, Science and Technology, Japan. We used the F-net broadband seismograms from the National Research Institute for Earth and Disaster Resilience (2019) and the earthquake catalogs from the Japan Meteorological Agency (https://www.data.jma.go.jp/svd/eqev/data/bulletin/index_e.html). OpenSWPC code Version 5.0.2 (Maeda et al., 2017) was utilized to calculate synthetic waveforms. We used the Fujitsu PRIMERGY CX600M1/CX1640M1 (Oakforest-PACS) at the Information Technology Center, the University of Tokyo for numerical simulations. Generic mapping tools (Wessel et al., 2013) and the Seismic Analysis Code (Helfrich et al., 2013) are used to prepare figures and process seismograms, respectively. Catalogs of shallow tremors detected by Yamashita et al. (2015; 2021) can be downloaded from the Slow Earthquake Database (Kano et al., 2018a). The estimated tremor energies and VLFE moments are provided in an open access repository, zenodo (https://doi.org/10.5281/zenodo.7226845).

Acknowledgements

We thank Ryosuke Ando, Aitaro Kato, Satoshi Ide, Asuka Yamaguchi, Shoichi Yoshioka, Takashi Tonegawa, Ryuta Arai, Masaru Nakano, Takane Hori, Eiichiro Araki, and Yojiro Yamamoto for their valuable discussions. We appreciate Youichi Asano for providing the shallow VLFE data in 2010. I also appreciate Azusa Nishizawa for providing the velocity structure data in Hyuga-nada. This research was supported by the JSPS KAKENHI Grant in Science Research on Innovative Areas “Science of Slow Earthquakes” (JP16H06472), Grant-in-Aid for Scientific Research on Transformative Research Areas (A) “Science of Slow-to-Fast earthquakes” (JP21H05205), and JSPS Research Fellowship DC1 (JP19J20760). This study was also supported by the ERI JURP 2021-S-B102. This research is part of Satoru Baba’s PhD thesis (Baba, 2022).

Declaration of competing interest

The authors declare that there are no competing interests.

References

Amante, C., & Eakins, B.W. 2009. ETOPO1 1 Arc-Minute Global Relief Model: Procedures, Data Sources and Analysis. NOAA Technical Memorandum NESDIS NGDC-24. https://doi.org/10.7289/V5C8276M

Ando, R., Takeda, N., Yamashita, T., 2012. Propagation dynamics of seismic and aseismic slip governed by fault heterogeneity and Newtonian rheology. Journal of Geophysical Research B: Solid Earth 117. https://doi.org/10.1029/2012JB009532

Aoi, S., Asano, Y., Kunugi, T., Kimura, T., Uehira, K., Takahashi, N., Ueda, H., Shiomi, K., Matsumoto, T., Fujiwara, H., 2020. MOWLAS: NIED observation network for earthquake, tsunami and volcano. Earth, Planets and Space 72. https://doi.org/10.1186/s40623-020-01250-x

Asano, Y., Obara, K., Matsuzawa, T., Hirose, H., Ito, Y., 2015. Possible shallow slow slip events in Hyuga-nada, Nankai subduction zone, inferred from migration of very low frequency earthquakes. Geophys Res Lett 42, 331–338. https://doi.org/10.1002/2014GL062165

Baba, S., 2022. Spatiotemporal characteristics of slow earthquakes in subduction zones around Japan. PhD thesis of the University of Tokyo, Japan.

Baba, S., Obara, K., Takemura, S., Takeo, A., Abers, G.A., 2021. Shallow Slow Earthquake Episodes Near the Trench Axis Off Costa Rica. J Geophys Res Solid Earth. https://doi.org/10.1029/2021JB021706

Baba, S., Takemura, S., Obara, K., Noda, A., 2020. Slow Earthquakes Illuminating Interplate Coupling Heterogeneities in Subduction Zones. Geophys Res Lett 47, 4–5. https://doi.org/10.1029/2020GL088089

Bartlow, N.M., Miyazaki, S., Bradley, A.M., Segall, P., 2011. Space-time correlation of slip and tremor during the 2009 Cascadia slow slip event. Geophys Res Lett 38. https://doi.org/10.1029/2011GL048714

DeMets, C., Gordon, R.G., Argus, D.F., Stein, S., 1994. Effect of recent revisions to the geomagnetic reversal time scale on estimates of current plate motions. Geophys Res Lett 21, 2191–2194. https://doi.org/10.1029/94GL02118

Dragert, H., Wang, K., James, T.S., 2001. A Silent Slip Event on the Deeper Cascadia Subduction Interface. Science (1979) 292, 1525–1528. https://doi.org/10.1126/science.1060152

Helffrich, G., Wookey, J., & Bastow, I. (2013). The Seismic Analysis Code. Cambridge: Cambridge University Press. https://doi.org/10.1017/CBO9781139547260

Hirose, H., Hirahara, K., Kimata, F., Fujii, N., Miyazaki, S., 1999. A slow thrust slip event following the two 1996 Hyuganada earthquakes beneath the Bungo Channel, southwest Japan. Geophys Res Lett 26, 3237–3240. https://doi.org/10.1029/1999GL010999

Houston, H., Delbridge, B.G., Wech, A.G., Creager, K.C., 2011. Rapid tremor reversals in Cascadia generated by a weakened plate interface. Nat Geosci 4, 404–409. https://doi.org/10.1038/ngeo1157

Ide, S., 2016. Characteristics of slow earthquakes in the very low frequency band: Application to the Cascadia subduction zone. J Geophys Res Solid Earth 121, 5942–5952. https://doi.org/10.1002/2016JB013085

Ide, S., Beroza, G.C., Shelly, D.R., Uchide, T., 2007. A scaling law for slow earthquakes. Nature 447, 76–79. https://doi.org/10.1038/nature05780

Ide, S., Maury, J., 2018. Seismic Moment, Seismic Energy, and Source Duration of Slow Earthquakes: Application of Brownian slow earthquake model to three major subduction zones. Geophys Res Lett 45, 3059–3067. https://doi.org/10.1002/2018GL077461

Ide, S., Yabe, S., 2014. Universality of slow earthquakes in the very low frequency band. Geophys Res Lett 41, 2786–2793. https://doi.org/10.1002/2014GL059712

Igarashi, T., 2020. Catalog of small repeating earthquakes for the Japanese Islands. Earth, Planets and Space 72. https://doi.org/10.1186/s40623-020-01205-2

Ito, Y., Obara, K., Shiomi, K., Sekine, S., Hirose, H., 2007. Slow Earthquakes Coincident with Episodic Tremors and Slow Slip Events. Science (1979) 315, 503–506. https://doi.org/10.1126/science.1134454

Kanamori, H., Anderson, D.L., 1975. THEORETICAL BASIS OF SOME EMPIRICAL RELATIONS IN SEISMOLOGY, Bulletin of the Seismological Society of America.

Kaneko, L., Ide, S., Nakano, M., 2018. Slow Earthquakes in the Microseism Frequency Band (0.1–1.0 Hz) off Kii Peninsula, Japan. Geophys Res Lett 45, 2618–2624. https://doi.org/10.1002/2017GL076773

Kano, M., Aso, N., Matsuzawa, T., Ide, S., Annoura, S., Arai, R., Baba, S., Bostock, M., Chao, K., Heki, K., Itaba, S., Ito, Y., Kamaya, N., Maeda, T., Maury, J., Nakamura, M., Nishimura, T., Obana, K., Ohta, K., Poiata, N., Rousset, B., Sugioka, H., Takagi, R., Takahashi, T., Takeo, A., Tu, Y., Uchida, N., Yamashita, Y., Obara, K., 2018a. Development of a Slow Earthquake Database. Seismological Research Letters 89, 1566–1575. https://doi.org/10.1785/0220180021

Kano, M., Kato, A., Ando, R., Obara, K., 2018b. Strength of tremor patches along deep transition zone of a megathrust. Sci Rep 8. https://doi.org/10.1038/s41598-018-22048-8

Katakami, S., Yamashita, Y., Yakihara, H., Shimizu, H., Ito, Y., Ohta, K., 2017. Tidal Response in Shallow Tectonic Tremors. Geophys Res Lett 44, 9699–9706. https://doi.org/10.1002/2017GL074060

Kato, A., Obara, K., Igarashi, T., Tsuruoka, H., Nakagawa, S., Hirata, N., 2012. Propagation of Slow Slip Leading Up to the 2011 Mw 9.0 Tohoku-Oki Earthquake. Science (1979) 335, 705–708. https://doi.org/10.1126/science.1215141

Koketsu, K., Miyake, H., Suzuki, H., 2012. Japan Integrated Velocity Structure Model Version 1. In: Proceedings of the 15th World Conference on Earthquake Engineering, Lisbon, Portugal, 24-28 September, Paper 1773.

Maeda, T., Takemura, S., Furumura, T., 2017. OpenSWPC: An open-source integrated parallel simulation code for modeling seismic wave propagation in 3D heterogeneous viscoelastic media 4. Seismology. Earth, Planets and Space 69. https://doi.org/10.1186/s40623-017-0687-2

Masuda, K., Ide, S., Ohta, K., Matsuzawa, T., 2020. Bridging the gap between low-frequency and very-low-frequency earthquakes. Earth, Planets and Space 72. https://doi.org/10.1186/s40623-020-01172-8

Nadeau, R.M., McEvilly, T. v, 1999. Fault Slip Rates at Depth from Recurrence Intervals of Repeating Microearthquakes, A. A. Koulakov and B. I. Shklovskii Phys. Rev. B.

Nakanishi, A., Takahashi, N., Yamamoto, Y., Takahashi, T., Citak, S.O., Nakamura, T., Obana, K., Kodaira, S., Kaneda, Y., 2018. Three-dimensional plate geometry and P-wave velocity models of the subduction zone in SW Japan: Implications for seismogenesis. Special Paper of the Geological Society of America 534, 69–86. https://doi.org/10.1130/2018.2534(04)

Nakano, M., Hori, T., Araki, E., Kodaira, S., Ide, S., 2018. Shallow very-low-frequency earthquakes accompany slow slip events in the Nankai subduction zone /704/2151/210 /704/2151/508 article. Nat Commun 9. https://doi.org/10.1038/s41467-018-03431-5

National Research Institute for Earth Science and Disaster Resilience, 2019. NIED F-net. https://doi.org/10.17598/NIED.0005

Nishizawa, A., Kaneda, K., Oikawa, M., 2009. Seismic structure of the northern end of the Ryukyu Trench subduction zone, southeast of Kyushu, Japan. Earth, Planets and Space 61, e37–e40. https://doi.org/10.1186/bf03352942

Obara, K., 2002. Nonvolcanic Deep Tremor Associated with Subduction in Southwest Japan. Science

(1979) 296, 1679–1681. https://doi.org/10.1126/science.1070378
Obara, K., Ito, Y., 2005. Very low frequency earthquakes excited by the 2004 off Kii peninsula earthquakes: A dynamic deformation process in the large accretionary prism. Earth, Planets and Space 57, 321–326. https://doi.org/10.1186/BF03352570
Obara, K., Kato, A., 2016. Connecting slow earthquakes to huge earthquakes. Science 353, 253–257. https://doi.org/10.1126/science.aaf1512
Ohta, K., Ide, S., 2017. Resolving the Detailed Spatiotemporal Slip Evolution of Deep Tremor in Western Japan. J Geophys Res Solid Earth 122, 10,009-10,036. https://doi.org/10.1002/2017JB014494
Rogers, G., Dragert, H., 2003. Episodic Tremor and Slip on the Cascadia Subduction Zone: The Chatter of Silent Slip. Science (1979) 300, 1942–1943. https://doi.org/10.1126/science.1084783
Sato, H., Fehler, M., Maeda, T., 2012. Seismic Wave Propagation and Scattering in the Heterogeneous Earth Structure, 2nd ed., New York, Springer-Verlag.
Shelly, D.R., Beroza, G.C., Ide, S., Nakamula, S., 2006. Low-frequency earthquakes in Shikoku, Japan, and their relationship to episodic tremor and slip. Nature 442, 188–191. https://doi.org/10.1038/nature04931
Skarbek, R.M., Rempel, A.W., Schmidt, D.A., 2012. Geologic heterogeneity can produce aseismic slip transients. Geophys Res Lett 39. https://doi.org/10.1029/2012GL053762
Takemura, S., Baba, S., Yabe, S., Emoto, K., Shiomi, K., Matsuzawa, T., 2022a. Source Characteristics and Along-Strike Variations of Shallow Very Low Frequency Earthquake Swarms on the Nankai Trough Shallow Plate Boundary. Geophys Res Lett 49. https://doi.org/10.1029/2022GL097979
Takemura, S., Matsuzawa, T., Noda, A., Tonegawa, T., Asano, Y., Kimura, T., Shiomi, K., 2019. Structural Characteristics of the Nankai Trough Shallow Plate Boundary Inferred From Shallow Very Low Frequency Earthquakes. Geophys Res Lett 46, 4192–4201. https://doi.org/10.1029/2019GL082448
Takemura, S., Obara, K., Shiomi, K., Baba, S., 2022b. Spatiotemporal Variations of Shallow Very Low Frequency Earthquake Activity Southeast Off the Kii Peninsula, Along the Nankai Trough, Japan. J Geophys Res Solid Earth 127. https://doi.org/10.1029/2021JB023073
Takemura, S., Okuwaki, R., Kubota, T., Shiomi, K., Kimura, T., Noda, A., 2020. Centroid moment tensor inversions of offshore earthquakes using a three-dimensional velocity structure model: slip distributions on the plate boundary along the Nankai Trough. Geophys J Int 222, 1109–1125. https://doi.org/10.1093/gji/ggaa238
Tonegawa, T., Yamashita, Y., Takahashi, T., Shinohara, M., Ishihara, Y., Kodaira, S., Kaneda, Y., 2020. Spatial relationship between shallow very low frequency earthquakes and the subducted Kyushu-Palau Ridge in the Hyuga-nada region of the Nankai subduction zone. Geophys J Int 1542–1554. https://doi.org/10.1093/gji/ggaa264

Uchida, N., Matsuzawa, T., Hasegawa, A., Igarashi, T., 2003. Interplate quasi-static slip off Sanriku, NE Japan, estimated from repeating earthquakes. Geophys Res Lett 30. https://doi.org/10.1029/2003GL017452

Vaca, S., Vallée, M., Nocquet, J.M., Battaglia, J., Régnier, M., 2018. Recurrent slow slip events as a barrier to the northward rupture propagation of the 2016 Pedernales earthquake (Central Ecuador). Tectonophysics 724–725, 80–92. https://doi.org/10.1016/j.tecto.2017.12.012

Wessel, P., Smith, W.H.F., Scharroo, R., Luis, J., Wobbe, F., 2013. Generic mapping tools: Improved version released. Eos (Washington DC) 94, 409–410. https://doi.org/10.1002/2013EO450001

Yabe, S., Baba, S., Tonegawa, T., Nakano, M., Takemura, S., 2021. Seismic energy radiation and along-strike heterogeneities of shallow tectonic tremors at the Nankai Trough and Japan Trench. Tectonophysics 228714. https://doi.org/10.1016/j.tecto.2020.228714

Yabe, S., Tonegawa, T., Nakano, M., 2019. Scaled Energy Estimation for Shallow Slow Earthquakes. J Geophys Res Solid Earth 124, 1507–1519. https://doi.org/10.1029/2018JB016815

Yamamoto, Y., Ariyoshi, K., Yada, S., Nakano, M., Hori, T., 2022. Spatio-temporal distribution of shallow very-low-frequency earthquakes between December 2020 and January 2021 in Kumano-nada, Nankai subduction zone, detected by a permanent seafloor seismic network. Earth, Planets and Space 74, 14. https://doi.org/10.1186/s40623-022-01573-x

Yamamoto, Y., Obana, K., Takahashi, T., Nakanishi, A., Kodaira, S., Kaneda, Y., 2013. Imaging of the subducted kyushu-palau ridge in the hyuga-nada region, western nankai trough subduction zone. Tectonophysics 589, 90–102. https://doi.org/10.1016/j.tecto.2012.12.028

Yamashita, Y., Asano, Y., Shimizu, H., Uchida, K., Hirano, S., Umakoshi, K., Miyamachi, H., Nakamoto, M., Fukui, M., Kamizono, M., Kanehara, H., Yamada, T., Shinohara, M., Obara, K., Yakiwara, H., Asano, Y., Shimizu, H., Uchida, K., Hirano, S., Umakoshi, K., Miyamachi, H., Nakamoto, M., Fukui, M., Kamizono, M., Kanehara, H., Yamada, T., Shinohara, M., Obara, K., 2015. Migrating tremor off southern Kyushu as evidence for slow slip of a shallow subduction interface. Science (1979) 348, 676–679. https://doi.org/10.1126/science.aaa4242

Yamashita, Y., Shimizu, H., Goto, K., 2012. Small repeating earthquake activity, interplate quasi-static slip, and interplate coupling in the Hyuga-nada, southwestern Japan subduction zone. Geophys Res Lett 39. https://doi.org/10.1029/2012GL051476

Yamashita, Y., Shinohara, M., Yamada, T., 2021. Shallow tectonic tremor activities in Hyuga-nada, Nankai subduction zone, based on long-term broadband ocean bottom seismic observations. Earth, Planets and Space 73, 196. https://doi.org/10.1186/s40623-021-01533-x

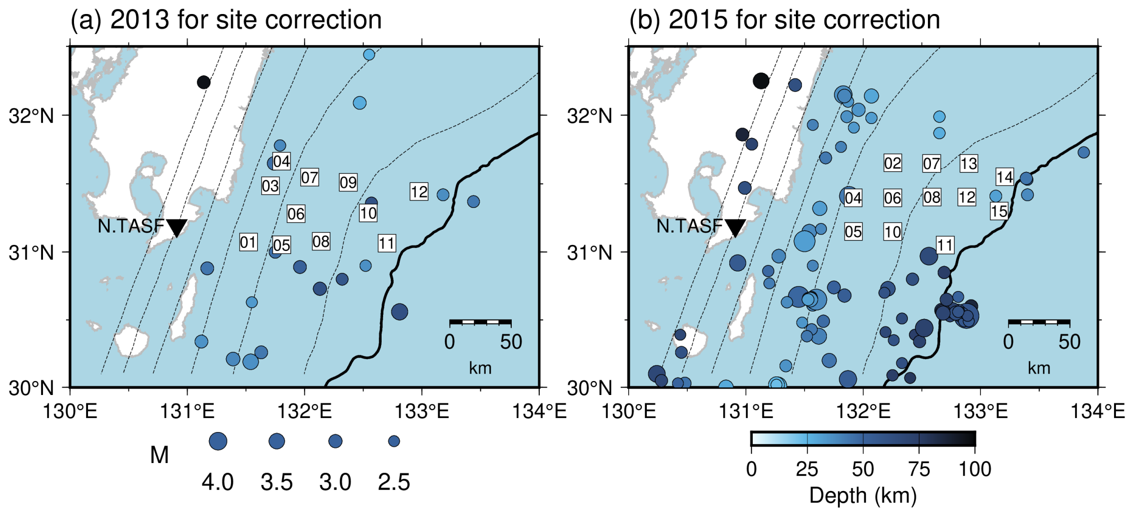

Fig. S1. Distribution of earthquakes used for the estimation of the site amplification factors. Inverted triangles display the locations of the F-net stations. Squares represents the locations of OBSs. Black line and dotted contours are the same as displayed in Fig. 6.

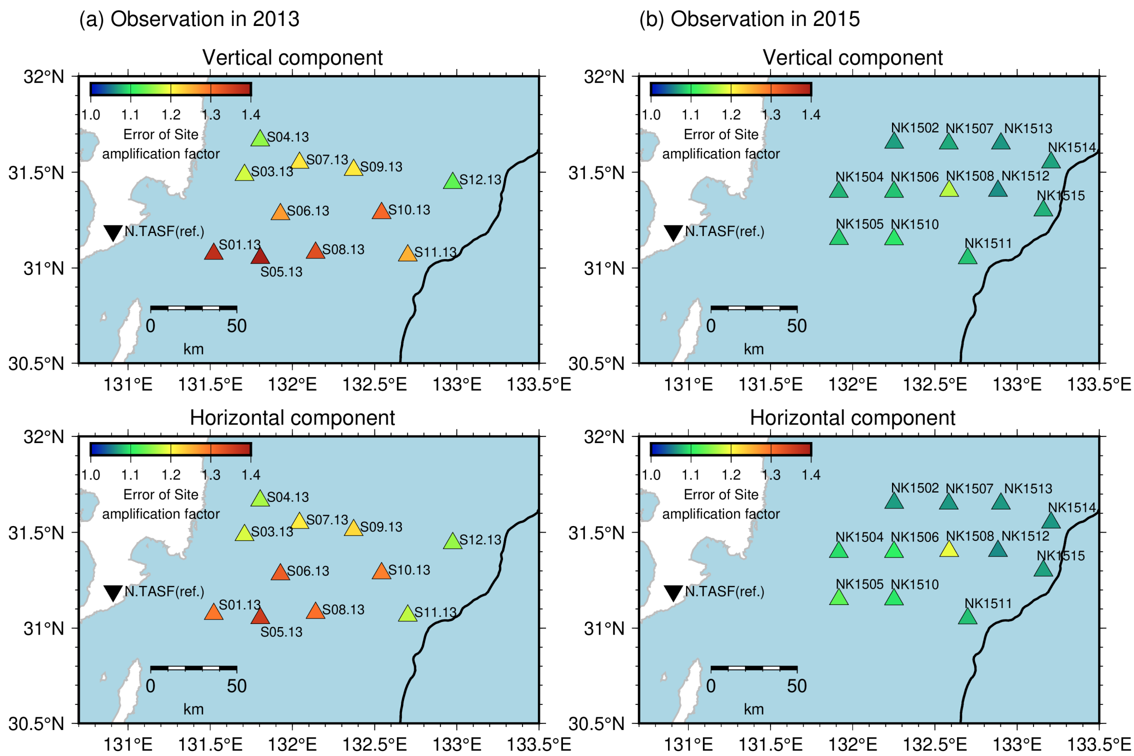

Fig. S2. Estimation errors of site amplification factors at each station. Inverted triangle indicates the location of the F-net station, N.TASF. Black line is the same as displayed in Fig. 3.

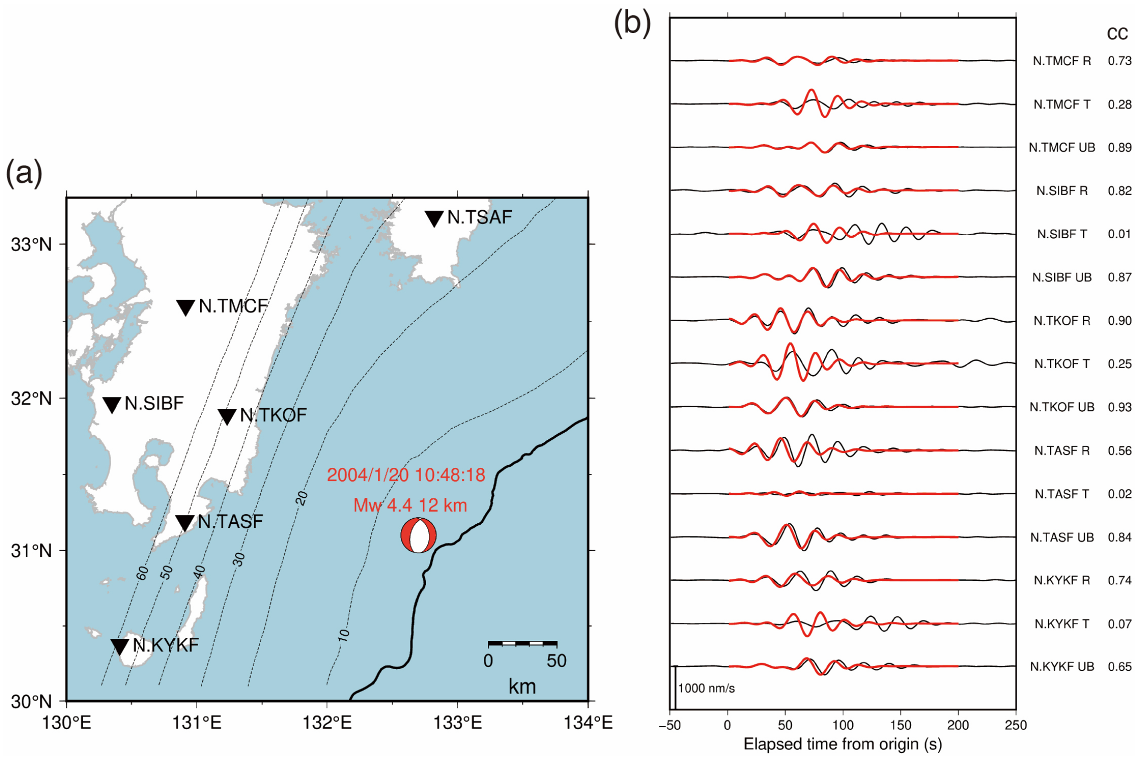

Fig. S3. Simulated waveforms of a regular earthquake that occurred in northern Hyuga-nada. (a) Focal mechanism of the regular earthquake listed in the catalog by Takemura et al. (2020; catalog: doi:10.5281/zenodo.3821172). Black line, inverted triangles, and dotted contours are the same as displayed in Fig. 6. (b) Observed (black lines) and simulated (red lines) waveforms of the earthquake at each F-net station. The assumed source time function was a Küpper wavelet with a source duration of 1 s. Black and red lines are the observed and the simulated waveforms, respectively. The simulation setting is the same as described in Section 2.2. R, T, and UB components represent the radial, transverse, and vertical components, respectively.

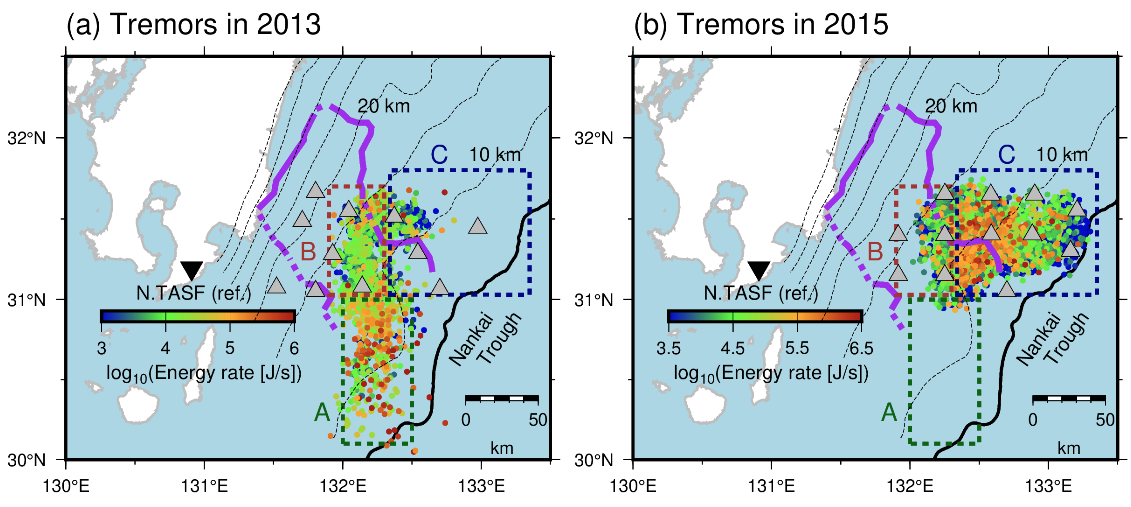

Fig. S4. Spatial distribution of energy rates of shallow tremors in (a) 2013 and (c) in 2015. Colored dotted rectangles, dashed contours, purple lines, black line and gray triangles are the same as displayed in Fig. 7.

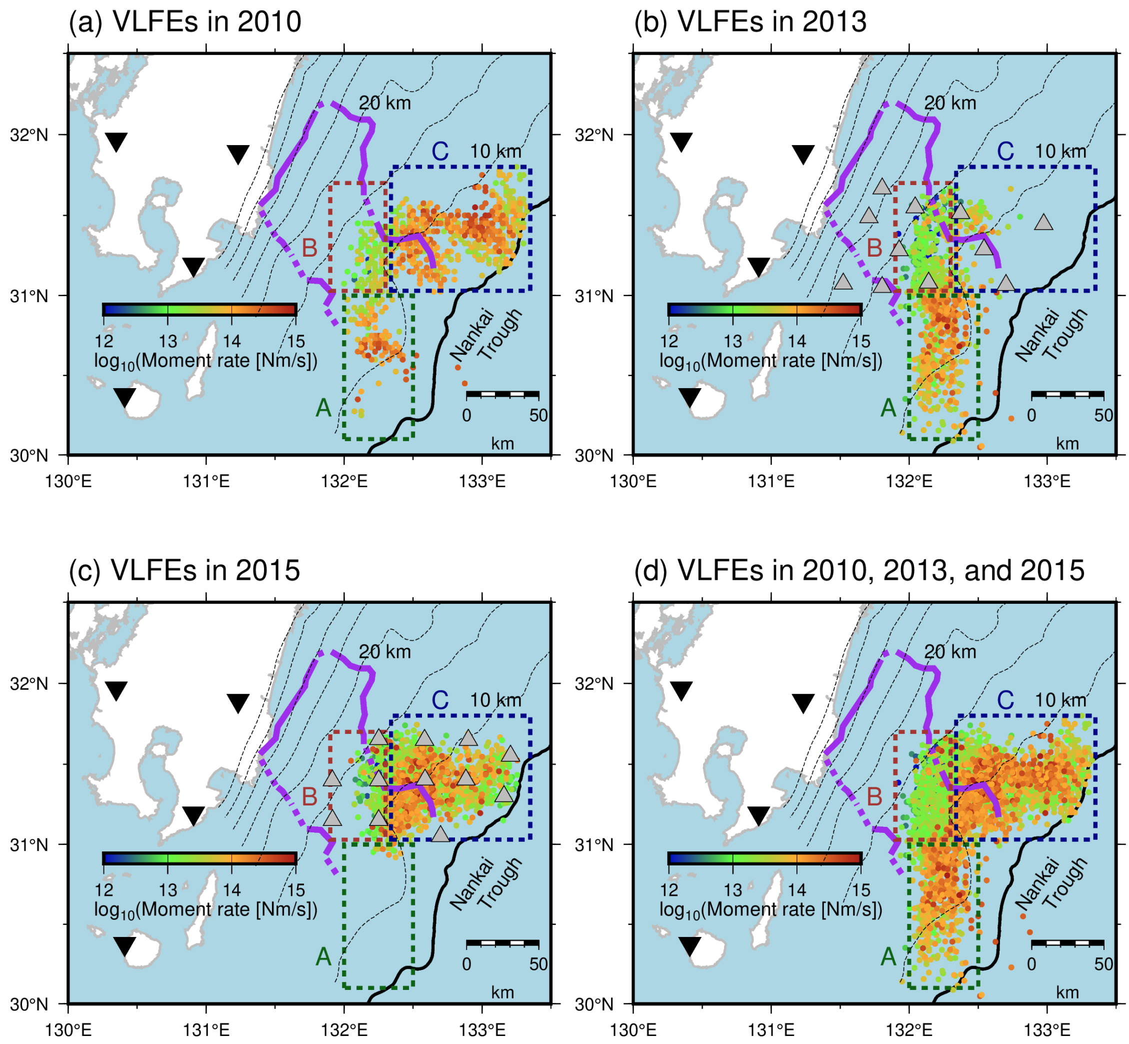

Fig. S5. Spatial distribution of moment rates of shallow VLFEs in (a) 2010, (b) 2013, (c) 2015, and (d) all analysis periods. Colored dotted rectangles, dashed contours, purple lines, black line and gray triangles are the same as displayed in Fig. 7.

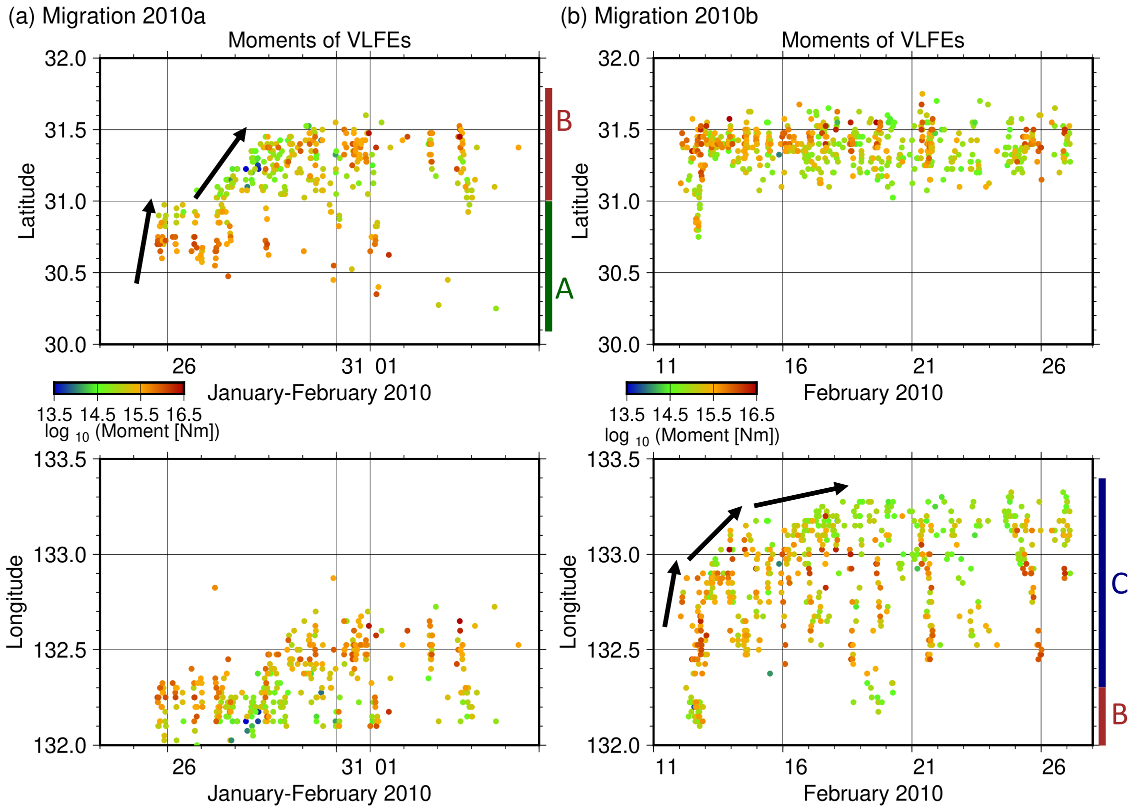

(a) Migration 2010a
Moments of VLFEs
Latitude
Longitude
January-February 2010
13.5 14.5 15.5 16.5
log 10 (Moment [Nm])
A
B
(b) Migration 2010b
Moments of VLFEs
Latitude
Longitude
February 2010
13.5 14.5 15.5 16.5
log 10 (Moment [Nm])
B
C

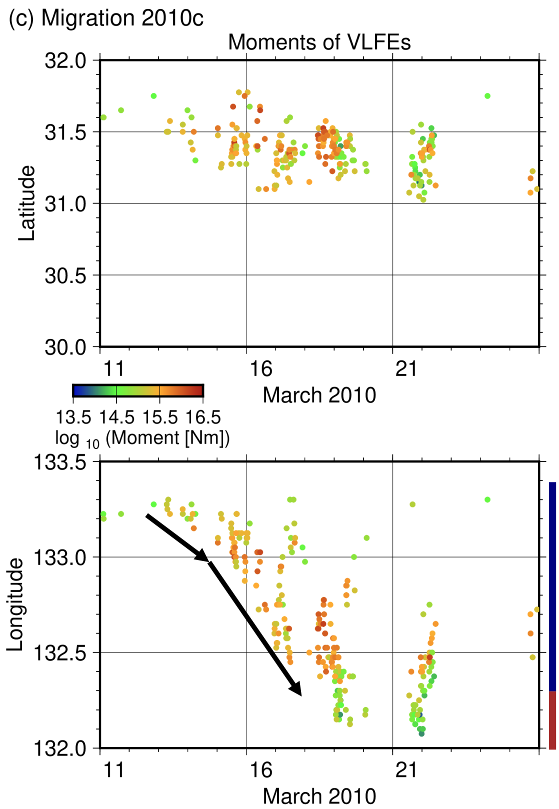

(c) Migration 2010c
Moments of VLFEs
Latitude
Longitude
March 2010
13.5 14.5 15.5 16.5
log 10 (Moment [Nm])
B
C

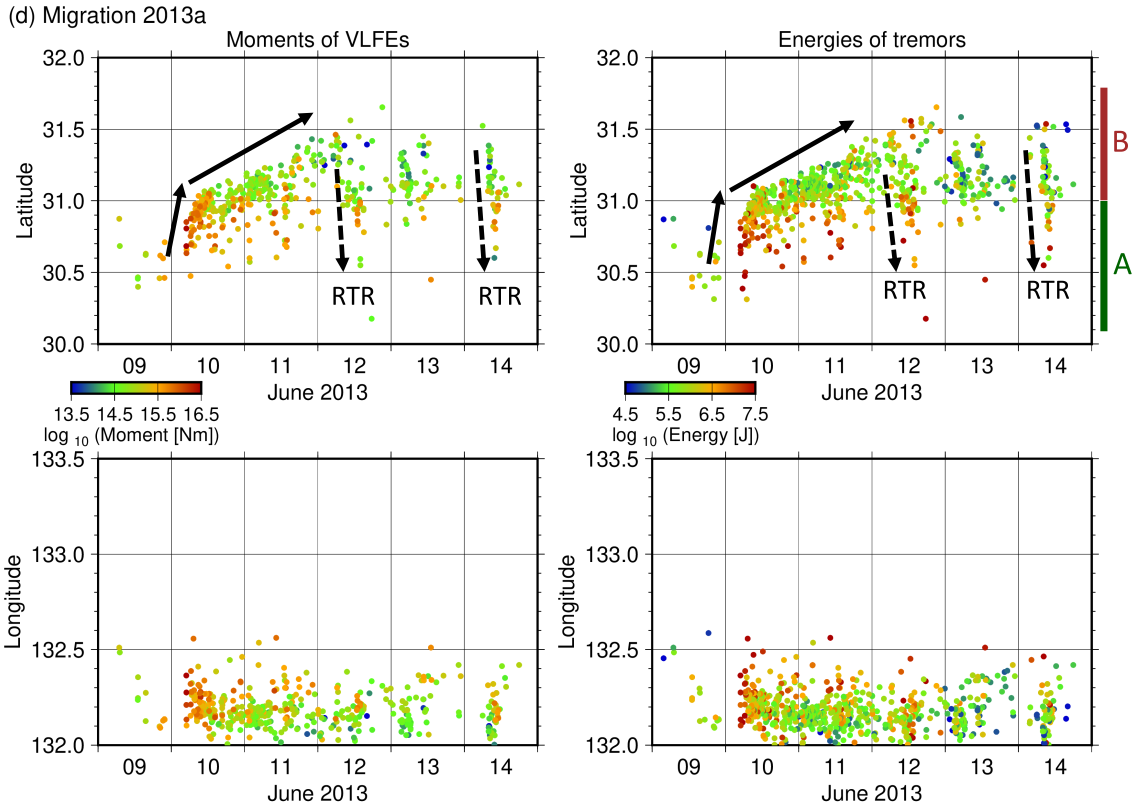
(d) Migration 2013a
Moments of VLFEs
Energies of tremors
Latitude
Longitude
RTR
RTR
RTR
RTR
B
A
June 2013
13.5 14.5 15.5 16.5
log 10 (Moment [Nm])
4.5 5.5 6.5 7.5
log 10 (Energy [J])

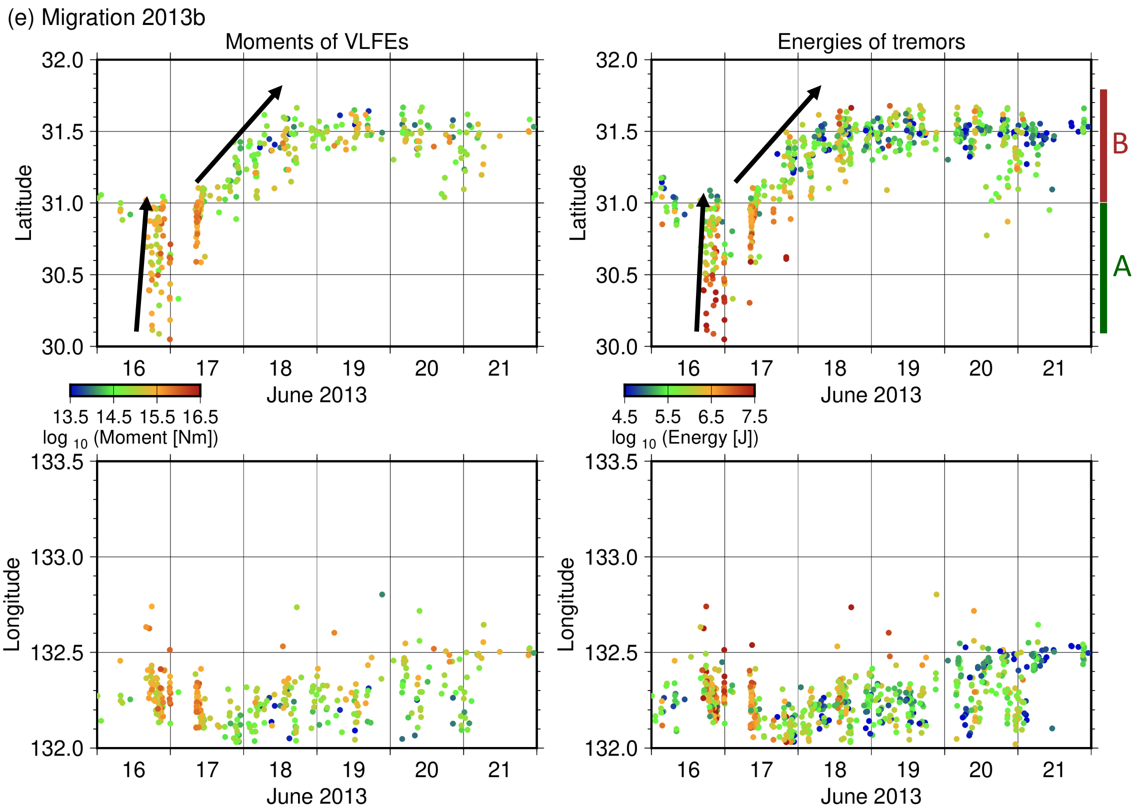
(e) Migration 2013b
Moments of VLFEs
Energies of tremors
Latitude
Longitude
B
A
June 2013
13.5 14.5 15.5 16.5
log 10 (Moment [Nm])
4.5 5.5 6.5 7.5
log 10 (Energy [J])

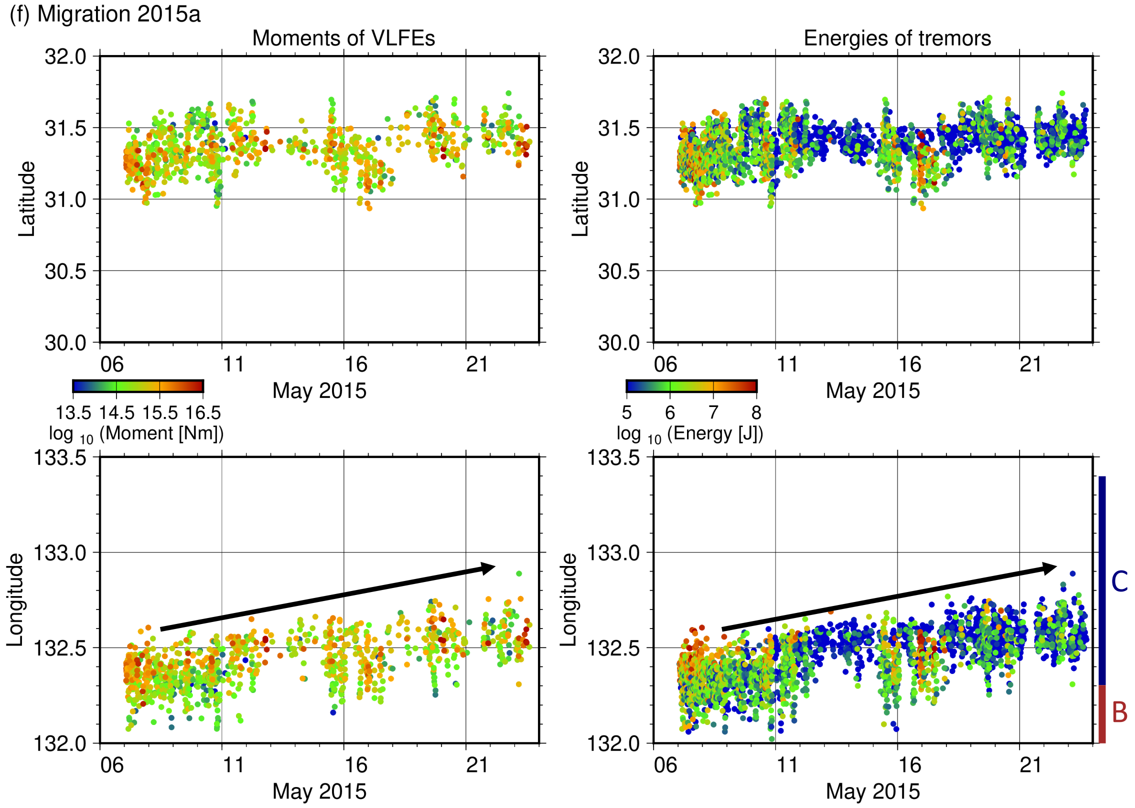
(f) Migration 2015a
Moments of VLFEs
Energies of tremors
Latitude
Longitude
May 2015
13.5 14.5 15.5 16.5
log 10 (Moment [Nm])
5 6 7 8
log 10 (Energy [J])
C
B

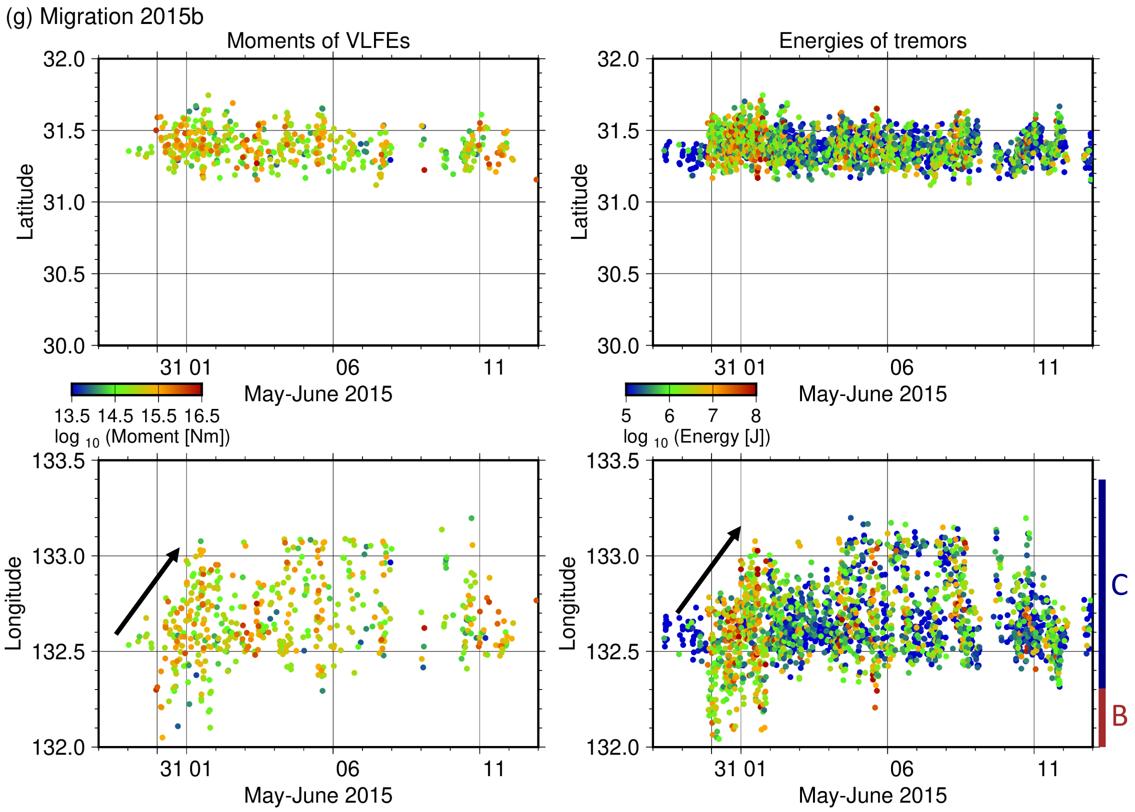
(g) Migration 2015b
Moments of VLFEs
Energies of tremors
Latitude
Longitude
May-June 2015
13.5 14.5 15.5 16.5
log 10 (Moment [Nm])
5 6 7 8
log 10 (Energy [J])
C
B

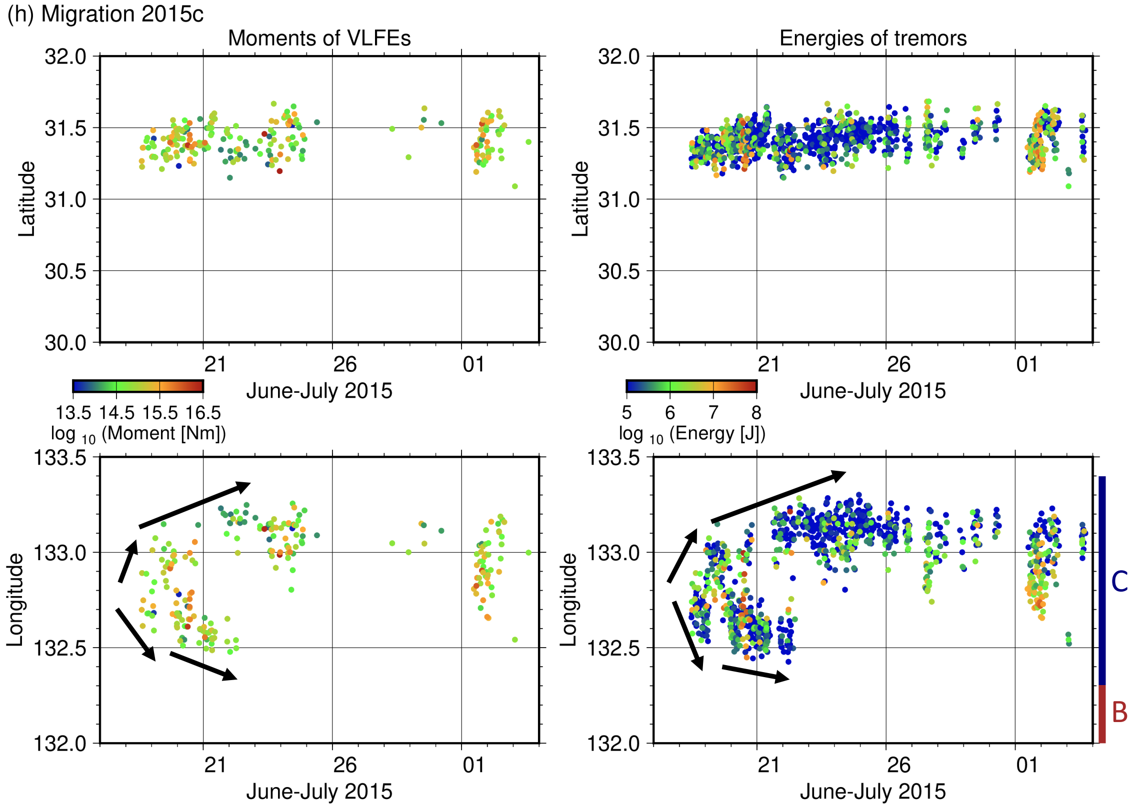

Fig. S6. Spatiotemporal distributions of moments of VLFEs and energies of tremors in the directions along the N-S and E-W sections for each migration. Black arrows indicate the direction of migrations. Black dotted arrows in Fig. S4d represents the RTR.

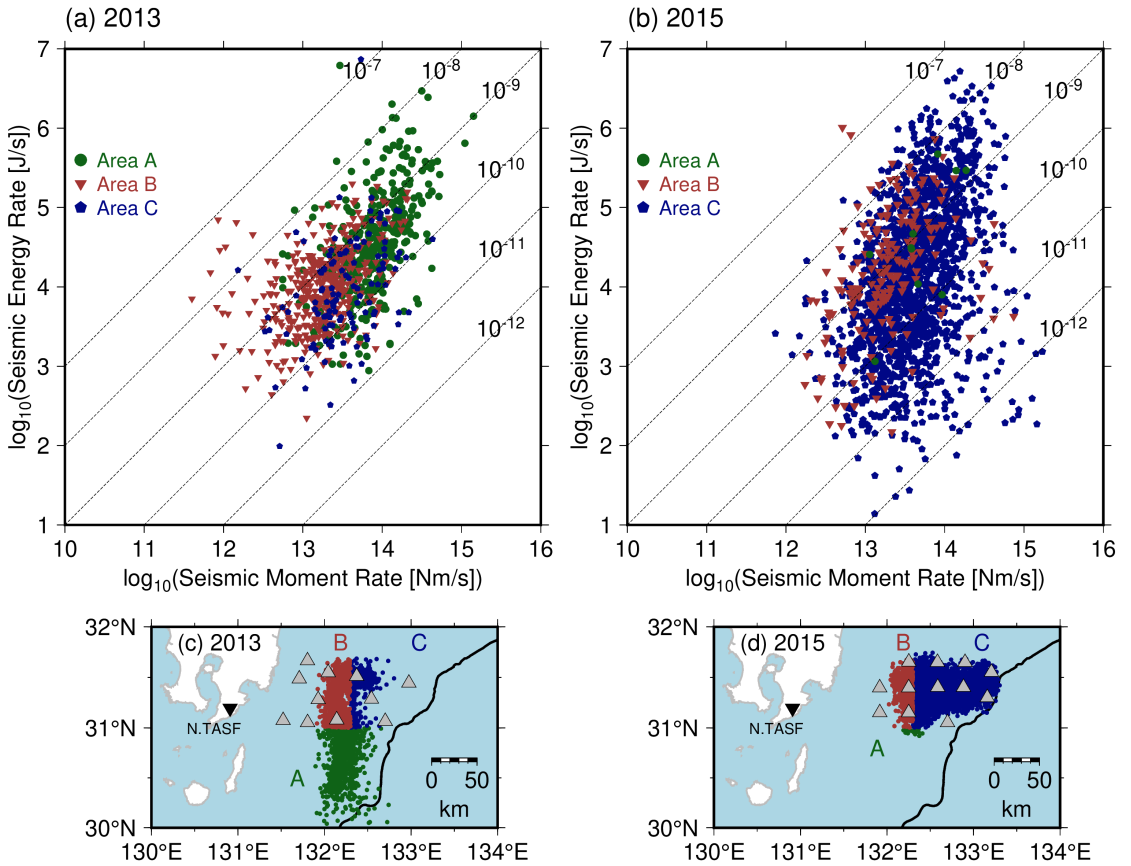

Fig. S7. Relationship between seismic moment rates of VLFEs and seismic moment rates of shallow tremors at each area in Hyuga-nada (a) in 2013 and (b) in 2015. Epicenters of shallow tremors at each area (c) in 2013 and (d) in 2015. Shallow tremors in Area A, B, and C are depicted by green, brown, and dark blue dots, respectably. Black lines, gray and black inverted triangles are the same as displayed in Fig.7.

Table S1. Characteristics of migrations in Hyuga-nada.

	Migration direction	
2010a	Along-strike	South to north
2010b	Along-dip	Downdip to updip
2010c	Along-dip	Updip to downdip
2013a	Along-strike	South to north
2013b	Along-strike	South to north
2015a	Along-dip	Downdip to updip
2015b	Along-dip	Downdip to updip
2015c	Along-dip	Bilateral